remote sensing

MDPI

Article

Versatile Fourier Transform Spectrometer Model for Earth Observation Missions Validated with In-Flight Systems Measurements

Tom Piekarski [1], Christophe Buisset [1,*], Anne Kleinert [2], Felix Friedl-Vallon [2], Arnaud Heliere [1], Julian Hofmann [1], Ljubiša Babić [1,3], Micael Dias Miranda [1], Tobias Guggenmoser [1], Daniel Lamarre [1], Flavio Mariani [1], Felice Vanin [1] and Ben Veihelmann [1]

[1] European Space Agency, 2201 AZ Noordwijk, The Netherlands; tomalexandrepiekarski@gmail.com (T.P.)
[2] Institut für Meteorologie und Klimaforschung, Karlsruher Institut für Technologie, 76131 Karlsruhe, Germany
[3] Aurora Technology B.V., 2201 AA Noordwijk, The Netherlands
* Correspondence: christophe.buisset@esa.int

Highlights

What are the main findings?

- We developed a unique and flexible Fourier transform spectrometer model that (i) simulates the instrument's signal and radiometric calibration and reconstructs the measured spectrum; (ii) estimates the radiometric performance; and (iii) predicts the instrument spectral response.
- The model has been successfully validated using the in-flight balloon-borne instrument GLORIA-Lite with a maximum deviation between the signal predictions and the measurements lower than 2%.

What are the implication of the main findings?

- We have successfully developed and validated an innovative model that accurately predicts the performance of future instruments based on Fourier transform spectrometers.
- This model will be used to optimise the design and analyse the performance of upcoming Fourier transform spectrometer-based payloads.

Abstract

Fourier transform spectrometers (FTSs) are cornerstone instruments in Earth observation space missions, effectively monitoring atmospheric gases in missions such as Michelson Interferometer for Passive Atmospheric Sounding (MIPAS), and Infrared Atmospheric Sounding Interferometer (IASI). It will also be the core instrument of Meteosat Third Generation—Sounding (MTG-S) and the future Earth Explorer (EE) mission Far-infrared Outgoing Radiation Understanding and Monitoring (FORUM). Building on this legacy, the European Space Agency (ESA) has developed an FTS instrument and an inverse model designed to estimate the radiometric and spectral performance from a set of instrumental parameters. The model and its validation using in-flight measurements of the FTS instrument Gimballed Limb Observer for Radiance Imaging of the Atmosphere (GLORIA)-Lite are described in this paper. The results indicate that the difference between the model predictions and the measured signal is less than 2% relative to the average of the measurements. Moreover, we can correctly predict the instrument's radiometric gain and offset and reconstruct a scientific science spectrum. This model can be utilised effectively to evaluate the radiometric performance of future FTS missions.

check for updates

Academic Editor: Prasad S. Thenkabail

Received: 23 October 2025
Revised: 26 November 2025
Accepted: 30 November 2025
Published: 30 November 2025

Citation: Piekarski, T.; Buisset, C.; Kleinert, A.; Friedl-Vallon, F.; Heliere, A.; Hofmann, J.; Babić, L.; Miranda, M.D.; Guggenmoser, T.; Lamarre, D.; et al. Versatile Fourier Transform Spectrometer Model for Earth Observation Missions Validated with In-Flight Systems Measurements. *Remote Sens.* **2025**, *17*, 3903. https://doi.org/10.3390/rs17233903

Copyright: © 2025 by the authors. Licensee MDPI, Basel, Switzerland. This article is an open access article distributed under the terms and conditions of the Creative Commons Attribution (CC BY) license (https://creativecommons.org/licenses/by/4.0/).

Keywords: Fourier transform spectrometer; instrument model; radiometric performance; radiometric calibration; spectrum reconstruction

1. Introduction

The Fourier transform spectrometer (FTS) presents the advantage of a high throughput and signal-to-noise ratio compared to dispersive or filter-based spectrometers [1,2]. For these reasons, FTSs have widely been used in previous Earth Observation (EO) missions to measure atmospheric trace gas concentrations. The Michelson Interferometer for Passive Atmospheric Sounding (MIPAS) developed by the European Space Agency (ESA) and launched in 2002 has observed the infrared limb emission spectrum [3]. The Infrared Atmospheric Sounding Interferometer (IASI), developed by the Centre national d'études spatiales (CNES) and operated by the European Organisation for the Exploitation of Meteorological Satellites (EUMETSAT), has measured, since 2006, the atmospheric temperature and water vapor profiles, as well as greenhouse gas concentrations [4]. The FTS constitutes the core instrument of the meteorological EUMETSAT—ESA mission Meteosat Third Generation—Sounding (MTG-S) [5], launched on 1 July 2025, and EUMETSAT—CNES IASI—New Generation (IASI-NG) [6], which was launched on 13 August 2025 onboard the MetOp-SG-A1 satellite. Several future Earth Explorer (EE) sounding and imaging ESA missions also integrate the FTS as their core instrument, such as EE9 Far-infrared Outgoing Radiation Understanding and Monitoring (FORUM) [7], EE11 candidates NITROSAT [8], and Changing-Atmosphere Infrared Tomography (CAIRT) [9] for applications such as limb sounding and the high-spatial-resolution detection of pollutants plumes.

ESA has identified the need for an FTS model for the performance prediction and design optimisation of future missions with the following objectives:

1. Predict the detected signal including the correct level of thermal background, dark current, and noise using a set of instrumental parameters as input;
2. Evaluate the instrument's radiometric performance;
3. Simulate the instrument radiometric calibration;
4. Reconstruct a scientific scene spectrum.

This model is intended to be used for the optimisation of critical FTS instrumental parameters, and to estimate the impact of instrumental errors on the radiometric and spectral performance. Additionally, the model will be used to assess the effects of the radiometric calibration strategy and interferogram processing on the quality of the reconstructed scene spectral radiance.

For these reasons, in the framework of an ESA graduate traineeship [10], we have developed an instrument model capable of producing interferograms that include signals both from the source and the instrument (thermal background and detector dark current), including noise sources, at a given pixel. The model accounts for signal generation based either on a photodetector or on a pyroelectric thermal detector. Errors affecting radiometric performance such as wavefront tilt, shear, wavefront error (WFE), and integration time effects are included. The self-apodisation effect is computed from the FOV geometry of the detector pixel. A key aspect of the model is the simulation of the instrument two-point radiometric calibration, with sources of reference radiances used for the reconstruction of the scientific scene spectral radiance, with the associated noise propagation. We have validated the model by using real in-flight data from the FTS Gimballed Limb Observer for Radiance Imaging of the Atmosphere (GLORIA)-Lite [11]. This model was internally reviewed by ESA experts from missions such as MTG-S, FORUM, CAIRT, and NITROSAT.

This paper is structured as follows: In Section 2, we compare the model capabilities with the state-of-the art FTS models. In Section 3, we give an overview of the instrument model and present the associated assumptions. The propagation and signal conversion of both the source and thermal background flux are described in Section 4. We focus in Section 5 on the instrumental errors and effects included in the interferogram calculation. The noise model and the associated radiometric budget are presented in Section 6. We describe the inverse model in Section 7. The validation of the instrument model with in-flight measurements is presented in Section 8. The validation of the inverse model through radiometric gain and offset in-flight data is described in Section 9. Finally, for an internal consistency check of the whole model chain, a reference limb spectrum reconstruction is presented in Section 10.

2. FTS Models State-of-the-Art

We have performed a review of the current state-of-the-art FTS models and compared their capabilities with the model. We extracted from this review nine models described in the literature from 1999 to 2024. Among this list, eight projects were developed by research institutes [12–19] and one by industry [20]. This selection includes models developed in European [18–20], American [12,13,17], Canadian [15,20], and Chinese [14,16] organisations.

The criteria used for the first part of this comparative study and listed in Table 1 are as follows:

1. Design flexibility: The model is suited for studying different instrumental designs and is not adapted to only one specific design. The optics architecture, performance, and temperature in the instrument can be modified without a source code update.
2. Scene generation: The model can generate a spectral radiance observed by the instrument from a set of atmospheric parameters and a radiative transfer model [21,22].
3. Scene temporal variation: The spectral content of the scene varies during the interferogram acquisition [23,24].
4. Photodetector: The model can provide signals assuming a photodetector and relying on a flux-to-signal conversion model [25].
5. Thermal detector: The model can provide signals assuming a thermal detector and relying on a flux-to-signal conversion model [25].
6. Interferogram simulation: The model can generate an interferogram sampled on an analogue or digitised axis.
7. Radiometric calibration: The model implements the observation of calibration sources, calculating calibration interferograms used to estimate the instrument gain and offset [26].
8. Spectrum reconstruction: The science scene spectrum is obtained from the science interferogram and the instrument radiometric gain and offset [26].

A model, developed at the Rochester Institute of Technology, uses the Digital Imaging and Remote Sensing Image Generation (DIRSIG) [12] to generate and propagate a temporal varying scene in the instrument to create an interferogram from a photodetector model only. The spectrum is reconstructed only by a Fourier transform of the associated interferogram. No radiometric calibration using reference sources is simulated. The same capabilities were found in a model developed at the same institute [13] which targets the airborne detection of fugitive gases, and in a simulator from the Chinese Academy of Sciences and the Hefei University of Technology [14], which is based on the spectrometer HJ1A-HSI that monitors Earth land and vegetation.

Table 1. Comparison between ESA and state-of-the-art FTS models extracted from literature: inputs, workflow, and outputs of each model. A green-filled tick indicates a capability, a pink-filled cross marks a feature that is not included, and a yellow minus sign denotes an effect that is only partially modelled or could be incorporated with limited-effort update.

Model	ESA	[12]	[13]	[14]	[20]	[15]	[16]	[17]	[18]	[19]
Design flexibility	✓	⊖	⊖	⊖	⊖	✓	✗	✓	✓	⊖
Scene generation	✗	✓	✓	✗	✗	✗	✗	✗	✓	✗
Scene temporal variation	⊖	✓	✓	✗	✗	✗	✗	✗	✗	✓
Photodetector	✓	✓	✓	✓	✓	✗	✗	✓	⊖	✗
Thermal detector	✓	✗	✗	✗	✗	✗	✗	✓	⊖	✓
Interferogram simulation	✓	✓	✓	✓	✓	⊖	⊖	✗	✓	✓
Radiometric calibration	✓	✗	✗	✗	✗	✗	✗	✗	✗	✗
Spectrum reconstruction	✓	⊖	⊖	✗	✗	✓	⊖	⊖	✗	✓

Based on the MIPAS heritage, a simulator for IASI has been developed by ABB which manufactured the mission interferometer [20]. It simulates an interferogram to predict IASI future performance and provide test data for the development of processing algorithms. However, the description of this simulator is limited to the interferogram realisation without any spectrum reconstruction. A generic model of the FTS spectral response, built in the frame of a doctoral thesis at Université Laval, is described in [15] but does not study the radiometric aspect of the instrument by modelling the optics or detector efficiencies. A Michelson interferometer simulator that was developed by the China Meteorological Administration, the Chinese Academy of Meteorological Sciences, and the Beijing University of Technology, based on the Geostationary Interferometric Infrared Imager (GIIRS), is presented in [16] to specifically study the effects of the pixel response non-linearity and off-axis angle on the spectrum. This model does not have the capabilities to estimate the instrument's radiometric performance, and the radiometric calibration is not simulated to compute the scene spectral radiance.

A numerical tool developed at the James Madison University, called Fourier Transform InfraRed Scientific Instrument Simulator (FTIR-SIS), is presented in [17]. It can generate a scene from a selection of atmospheric molecules and simulate two different predefined materials for the gas cell window, the beam splitter plates, and the detector window. One can also choose between two predefined photoconductor or thermal detector responses. However, only the spectral flux incident on the detector is visible. No interferogram is simulated and no science spectral radiance is reconstructed. The instrument radiometric performance cannot be estimated from FTIR-SIS. An E2E instrument simulator of the concept of Far Infra-Red Interferometer (FIRI) has been developed at the University College London and Leiden Observatory [18]. It specifically targets the observation of sub-arcsecond astronomical objects such as circumstellar disks. The scene reconstruction is performed using the CLEAN algorithm which is a method developed for radio astronomy. No radiometric calibration is simulated. Finally, a Simulator for the Herschel Imaging Fourier Transform Spectrometer (SHIFTS) model has been developed at the University of Lethbridge the and the Rutherford Appleton Laboratory, based on the Spectral and Photometric Imaging Receiver (SPIRE) which was observing in the FIR and millimetre band [19]. Only the SPIRE

bolometer detection technology is modelled, and, as in [18], no radiometric calibration is simulated.

We now focus the comparative analysis on criteria relative to the instrumental effects, error, and noise listed in Table 2 and defined as follows:

1. Instrument thermal background: The thermal self-emission of the instrument is considered to calculate the output signal and/or the noise levels.
2. Interferometer modulation losses: The wavefront error (WFE), tilt, and shear between the wavefront recombined in the interferometer are considered to calculate the performance [27].
3. Self-apodisation: The self-apodisation induced by the optical path difference in-field variation is considered to assess the performance and to calculate the output signal [28].
4. Detector non-linearity: The non-linearity of the detector response is considered to calculate the output signal [29].
5. PRNU: The pixel response non-uniformity (PRNU) [30] is considered to calculate the output signal.
6. Integration time effect: The impact of the integration time on the interferogram contrast effect due to the flux temporal integration is considered to calculate the output signal and the radiometric performance [31].
7. LOS jitter error: Jitter due to fluctuation of the line of sight (LOS) during the observation of an inhomogeneous scene is considered to estimate the output signal and the radiometric performance [32].
8. Sampling error: The non-regular sampling induced by the dynamic mirror displacement velocity variations is considered to calculate the output signal and the radiometric performance [33].

Table 2. Comparison between ESA and state-of-the-art literature FTS models: instrumental effects and errors. A green-filled tick indicates a capability, a pink-filled cross marks a feature that is not included, and a yellow minus sign denotes an effect that is only partially modelled or could be incorporated with limited-effort update.

Model	ESA	[12]	[13]	[14]	[20]	[15]	[16]	[17]	[18]	[19]
Instrument thermal background	✓	✗	✗	✗	✓	✗	✗	✗	✓	✓
Interferometer modulation losses	✓	✗	✗	✗	✓	✓	✗	✗	✗	✗
Self-apodisation	✓	✗	✗	✗	✓	✓	✓	✗	✗	✗
Detector non-linearity	✓	✗	✗	✗	✓	✗	✓	✗	✗	✗
Detector noise	✓	✓	✓	✓	✓	✗	✗	✗	✓	✓
PRNU	⊖	✓	✓	✓	✓	✓	✗	✗	✗	✗
Integration time effect	✓	✗	✗	✓	✓	✗	✗	✗	✗	✗
LOS jitter error	✗	✓	✓	✗	✗	✗	✗	✗	✓	✓
Sampling error	✗	✓	✓	✓	✓	✗	✗	✗	⊖	✓

The instrument thermal background, critical in the IR range, is only considered in the IASI [20], FIRI [18], and SPIRE [19] simulation models, as the first one targets the long-wave infrared scene and the two other are sensitive to the FIR. The other models do not include this contribution either because (1) they primarily focus on the impact of effects

such as PRNU, sampling errors, and LOS jitter errors as in the DIRSIG and the GIIRS-based models [12,16], (2) they study a spectral band where this contribution is negligible as in SHIFTS [19], or (3) they are not developed to estimate the instrument radiometric performance as in the spectral response model, the GIIRS simulator, and FTIR-SIS [15–17] which is why they do not consider the detector noise. The interferometer modulation losses resulting from imperfect surfaces and alignments in the interferometer which reduce the integrated spectral flux [27] are taken into account in the IASI simulator and FTIR-SIS [15,20]. The effect of the temporal integration of the flux during the signal acquisition is modelled in the HJ1A-HIS and the IASI models [14,20]. The effect of the detector response non-linearity is only included in the IASI and the GIIRS models [16,20].

Based on the listed model capabilities, we estimate that the IASI simulator [20], the FIRI model [18], and SHIFTS [19] can be used for the evaluation of an FTS radiometric performance as they both consider the instrument thermal background and the detector noise. However, these last two models are designed for specific astronomical applications in the FIR and mm range. They do not consider errors such as shear, tilt, and WFE which impact radiometric performance. The IASI simulator [20] includes these effects and appears to be the most flexible model for a radiometric budget evaluation. However, the description of this model stops at the generation of the interferogram. No reconstruction of a scene spectral radiance is presented. The instrument's spectral performance, impacted by self-apodisation, is thus not visible on the spectrum. Spectral performance can be evaluated with the dedicated model developed at Université Laval [15] which focuses on this aspect and considers radiometric performance out of its scope. In general, the effect of self-apodisation on the spectrum is also studied in the IASI and the GIIRS models [16,20].

One key aspect of this study is also the validation of these models. Among the nine communications we cited, three mentioned a validation. The IASI simulation model validation is based on the heritage of an FTS simulator developed for MIPAS at ABB Bomem [20], but no related communication is available in the literature. The SHIFTS model results have been compared with real HERSHEL-SPIRE measured spectra [19]. This comparison showed a correspondence between the simulated and real data of the SPIRE second band (31 cm^{-1}–55 cm^{-1}), but there is an important difference in the first band (14 cm^{-1}–34 cm^{-1}) where the "synthetic" (modelled) spectra contain up to five times more energy than the observed real data. A comparison between the spectral response model described in the Université Laval model [15] and real instrument line shape (ILS) measurements validated this model. But, as previously mentioned, only the spectral performance of the instrument is studied.

We notice that state-of-the-art models designed to be flexible, as with DIRSIG, the airborne FTS model from the Rochester Institute of Technology, and the IASI simulator [12,13,20], either do not simulate the instrument radiometric calibration and spectrum reconstruction [20], or do not consider key effects as thermal background [12,13]. This last point prevents us from evaluating the radiometric performance in and near the IR range. Some other reviewed models as the FIRI simulator and SHIFTS include errors we do not consider in the model as the LOS jitter and the sampling errors [18,19]. We did not include these effects as, in our applications, they were minor contributors to the radiometric performance budget compared to the noise and error contributions detailed in Sections 5 and 6. These last two models were developed to assess the performance of a specific instrument design and application as millimetric astronomy. Finally, only limited communication is made about the validation of these models.

We have combined six major innovations and novelties in the model developed at ESA. First, the model can be adapted to different instrument designs. For example, it has been used to simulate the configurations of CAIRT [34], GLORIA, GLORIA-B [35], and GLORIA-

Lite (see Sections 8 and 9), each of which features different apertures, interferometer configurations, spectral filters, operating temperatures, and front and back optics. Second, this model provides the capability to either use a photodetector or a thermal detector and is thus suitable for a large spectral domain from ultraviolet (UV) to FIR. Third, it uniquely combines the reconstruction of a scene spectrum based on the instrument's radiometric calibration with the realistic simulation of noisy interferograms from three different sources. The instrument and inverse models, along with their associated Python 3.9 code, can be run independently or collectively to simulate three interferogram acquisitions and reconstruct the science spectrum with a single execution. This facilitates the use of the model to perform an error analysis as we proceed in Section 8, and further to evaluate the instrument absolute radiometric accuracy [36]. Finally, this model predicts the level of the signal's minimum, maximum, and average levels with an accuracy better than 2%, as shown in Section 8.2.

3. Instrument Model

3.1. Instrument Model Overview and Assumptions

Figure 1 represents the instrument model block diagram. The input is a spectral radiance from either a scientific source provided by an atmospheric radiative transfer code, or a known calibration source such as a blackbody. The instrument model comprises the following sub-systems: the scan mirror, the front telescope (FT), the interferometer assembly (IA), the back telescope (BT), the spectral filter, the cryostat window (CW), the detection unit (DU) and the analogue-to-digital converter (ADC). The flux at the instrument output is converted into a signal by the DU which also adds the dark signal (in case of a photodetector) and the noise. The signal provided by the DU is digitised by the ADC that provides as outputs the scientific and calibration signals.

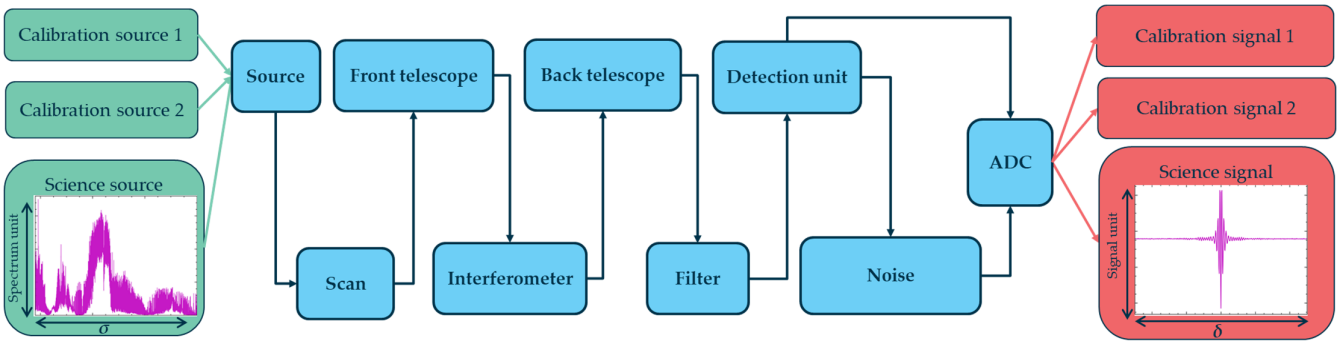

Figure 1. Instrument model architecture with the inputs filled in green, the outputs filled in red and the instrument model parts in blue.

The model can simulate a filter positioned either in the cryostat (Figure 2) or between the BT and the CW. The input beam is incident on the scan mirror that reflects the beam toward the FT and the IA that comprises a beam-splitting unit (BSU), and two cube corners CC1 (static) and CC2 (dynamic). The BSU reflects a fraction of the incident beam towards CC1 and transmits the other fraction toward CC2. During the data acquisition, CC2 is translated at the optical speed v_{opt} defining the optical path difference (OPD) scanning rate. For a duration Δt, the associated scanned OPD range is thus $v_{opt} \times \Delta t$. The beams reflected by CC_1 and CC_2 are incident on the BSU and transmitted and reflected toward the BT, respectively. The recombined beams transmitted by the BT are focused on the DU and pass by the CW, the spectral filter. The intermediate pupil Φ_I is located at the CC1 apex and the entrance pupil Φ_E is located at the scan mirror vicinity. The aperture stop is located at the detector box entrance and reimaged on the cube-corner apex. The detector is the system field stop.

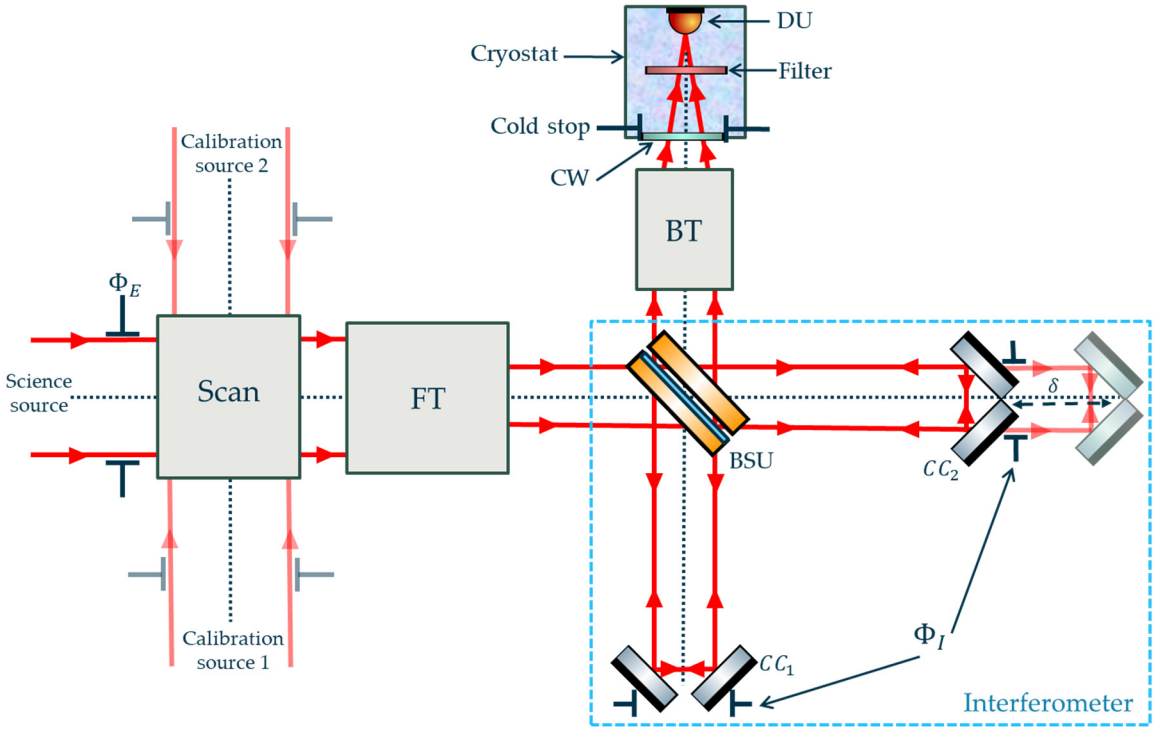

Figure 2. Instrument schematic with the optical rays and axis marked as red arrows and dashed lines. The movement of only one CC is represented in this figure. This sketch was created using the Component Library by Alexander Franzen, licensed under CC BY-NC 3.0.

We consider a step-and-stare observation method [37], with the barycentre of each pixel projected on the scene being static during the signal acquisition. The aberrations of the pupil imaging are considered negligible. Each optical sub-system is aplanatic, with a transmission K and an operating temperature T. The optical etendue is conserved through the instrument [38]. We neglect the contribution to the measured flux of the spurious reflections on the interferometer BSU plates, the CW, the filter, and the detector faces. The BSU comprises a beam-splitting surface (BS), a beam-splitting plate (BP), and a compensation plate (CP). The BP is coated with anti-reflective (AR) coating on one side and BS coating on the other, while the CP is AR-coated on both faces.

We assume that an ideal metrology correction is applied on the interferogram such that (1) the CC displacement is linear, and (2) the interferograms are regularly sampled and centred on the zero-path difference (ZPD). The detector is assumed to be photoconductive or pyroelectric. The photodetector noise budget comprises the following contributors: source, instrument thermal background and dark current shot noises, readout noise, ADC digitisation noise, and Johnson [25] and KTC [39] noises. The pyroelectric detection unit noise budget comprises the ADC digitisation noise, the detector noise, and the amplifier noise. The detector and amplifier noise can be provided by the manufacturer. In this case, the "detector noise" mainly includes the thermal fluctuation noise and the Johnson noise and is thus rather independent from the source [40].

3.2. Beam-Splitting Unit Model

The BSU model is represented in Figure 3 and allows simulating various BSU architectures [41]. A perfect, non-absorbing, zero-thickness BS plate is positioned at the centre. The BP and CP are divided into two plates called P1 and P2 (for BP) and P3 and P4 (for CP). It is important to notice that P1 and P2 (for BP) and P3 and P4 (for CP) have the same

thickness (h_{BP} for BP and h_{CP} for CP), orientation, and material characteristics as BP and CP, respectively. We disregard any spurious reflections on their surfaces.

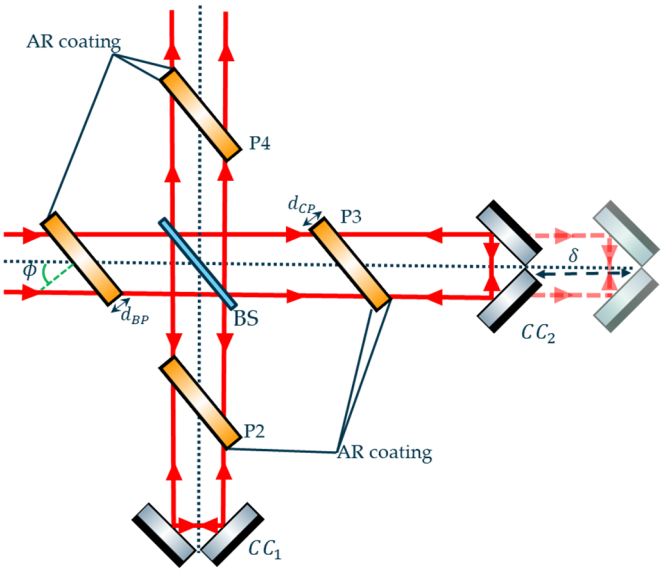

Figure 3. Instrument schematic with the optical rays and axis marked as red arrows and dashed lines. The movement of only one CC is represented in this figure. This sketch was created using the Component Library by Alexander Franzen, licensed under CC BY-NC 3.0.

The absorption of each plate α is determined by the material absorption rate β per unit of optical thickness h:

$$\alpha(\sigma) = e^{-h(\sigma)\beta(\sigma)} \tag{1}$$

where σ is the wavenumber. The crossed thickness of each plate depends on the mechanical thickness d, the beam incidence angle ϕ, and the material optical index n:

$$h(\sigma) = \frac{d}{\cos\left[\sin^{-1}\left[\frac{\sin\phi}{n(\sigma)}\right]\right]} \tag{2}$$

3.3. Detector Model

3.3.1. Photodetector Signal

For a spectral flux incident on a detector F, the photodetector flux-to-signal conversion is characterised by the pixel fill-factor ρ, the integration time τ_{int}, the detector quantum efficiency (QE) η, and the energy of a photon $hc\sigma$. The unmodulated (DC) signal N_{DC} associated to an unmodulated spectral flux F_{DC} is expressed as follows:

$$N_{DC} = \rho\tau_{int}\int \frac{\eta(\sigma)}{hc\sigma} F_{DC}(\sigma)d\sigma \tag{3}$$

The modulated (AC) signal N_{AC} associated to a modulated spectral flux F_{AC} is expressed as follows:

$$N_{AC}(\delta) = \rho\tau_{int}\mathrm{O}(\delta)\int \frac{\eta(\sigma)}{hc\sigma} M(\sigma)F_{\mathrm{AC}}(\sigma)\cos(2\pi\sigma\delta)d\sigma \tag{4}$$

$$N_{AC}(\delta) = \rho\tau_{int}\mathrm{O}(\delta)\Re\left\{FT\left[\frac{\eta(\sigma)}{hc\sigma} M(\sigma)F_{\mathrm{AC}}(\sigma)\right]\right\} \tag{5}$$

where δ is the OPD and $R\{FT\}$ denotes the real part of the Fourier transform. The quantities O and M are the instrument function and modulation efficiency which are described later in Section 5. This approach is valid both for the incident source and background flux.

Section 4.1 provides a comprehensive explanation of the source flux calculation through Equations (15)–(23). Detailed calculations for each background flux contributor are presented in Section 4.2, using Equations (24)–(38) for all instrument subsystems, apart from the IA self-emission, which is specifically addressed in Appendix A by Equations (A1)–(A16).

The dark signal N_{dark} depends on the detector dark current density I_{dark}, the horizontal and vertical pixel pitch (p_x,p_y), the Coulomb charge q, and the integration time:

$$N_{dark} = \frac{I_{dark} p_x p_y \tau_{int}}{q} \tag{6}$$

The total photonic signal N_{ph} is the sum of the modulated and unmodulated source N_s, background N_{bg}, and dark signals N_{dark} (Figure 4 left panel):

$$N_{ph}(\delta) = N_{s,DC} + N_{s,AC}(\delta) + N_{bg,DC} + N_{bg,AC}(\delta) + N_{dark} \tag{7}$$

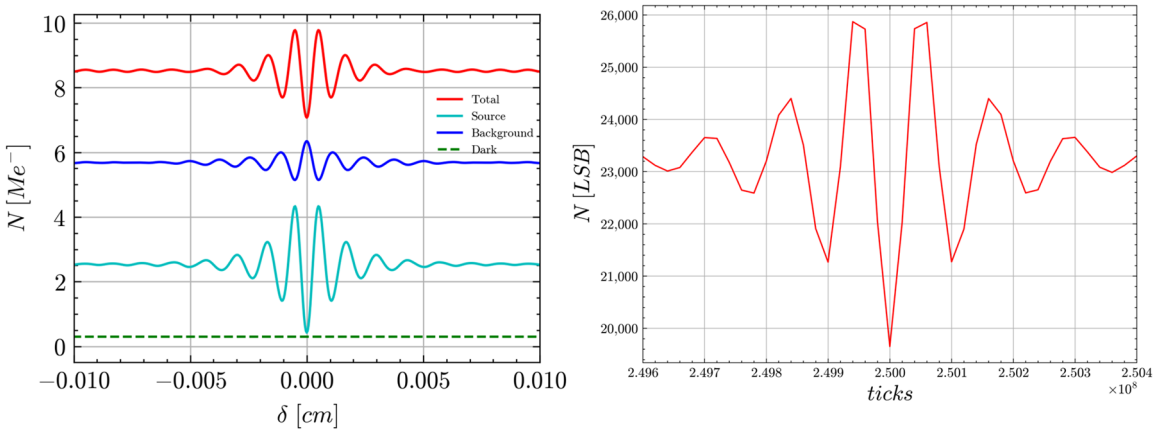

Figure 4. Photonic and digitised signals. (**Left panel**) Decomposition of photonic signal (red) into source (cyan), thermal background (blue), and dark signal (dashed green) before detector sampling. (**Right panel**) Sampled digitised signal.

3.3.2. Pyroelectric Detector Signal

A pyroelectric detector is only sensitive to the modulated signal [25]. The flux-to-signal conversion is modelled using the detector voltage response R_V and material absorbance α_{pyr}. The voltage response depends on the electric frequency f_{el} which, for an FTS, has a direct relation with the wavenumber σ. Using the optical speed v_{opt}, we can write $\sigma = f_{el}/v_{opt}$ (Equation 2.11 in [2]) and express the pyroelectric signal equation with the wavenumber:

$$N(\delta) = O(\delta) \int R_V(\sigma) \alpha_{pyr}(\sigma) M(\sigma) F_{AC}(\sigma) cos(2\pi\sigma\delta) d\sigma \tag{8}$$

$$N(\delta) = \mathrm{O}(\delta) \Re\{FT[R_V(\sigma)\alpha_{pyro}(\sigma)M(\sigma)F_{AC}(\sigma)]\} \tag{9}$$

The total signal converted by the pyroelectric detector N_{pyr} is the sum of the modulated source and background signals.

$$N_{pyr}(\delta) = N_{s,AC}(\delta) + N_{bg,AC}(\delta) \tag{10}$$

3.3.3. Signal Digitisation and Sampling

The total photonic or voltage signal, either described by Equation (7) or (10), respectively, is sampled according to the detector's acquisition framerate f_{acq} and the optical speed such that the OPD sample size equals v_{opt}/f_{acq}. The ADC digitises the signal according to its bit resolution, the charge handling capacity (CHC) in the specific case of a photodetector, and the maximum voltage swing for a pyroelectric detector. Figure 4's right panel shows

the sampled digitised signal in least significant bits (LSBs) obtained from the total photonic signal in mega electrons of the left panel.

3.3.4. Non-Linearity

The detector response NL is defined as the relative difference between the signal that would be provided by a detector with an ideal linear response N_E and the actual detected signal N [42,43]:

$$N(\delta) = N_E(\delta) \times (1 + NL(N_E)) \tag{11}$$

where the NL function is modelled as a third-order polynomial characterised by the coefficients $\{a_0; a_1; a_2; a_3\}$:

$$NL(N_E) = 1 - \left(a_0 + a_1 N_E + a_2 N_E^2 + a_3 N_E^3\right) \tag{12}$$

For a detector with an ideal linear response, the coefficient a_0 equals one and the others equal zero.

3.3.5. Noise Budget

The noise budget for the photodetector model includes the standard deviation of (1) the source shot noise $\xi_{shot,s}$, (2) the background shot noise $\xi_{shot,bg}$, (3) the dark shot noise ξ_{dark}, (4) the readout noise ξ_{read}, (5) the Johnson noise ξ_{John}, (6) the KTC noise ξ_{KTC}, and (7) the ADC digitisation noise ξ_{ADC}. These noises are considered independent such that the total noise variance ξ^2 is the quadratic sum of all its contributors. We also include in the noise budget the factors of pixel spatial binning b_{spat} and acquisitions temporal averaging b_{temp}. The expression of the standard deviation of the total noise detected by the photodetector DU is, thus, as follows:

$$\xi_{ph} = \sqrt{\frac{\xi_{shot,s}^2 + \xi_{shot,bg}^2 + \xi_{dark}^2 + \xi_{read}^2 + \xi_{John}^2 + \xi_{KTC}^2 + \xi_{ADC}^2}{b_{spat} \times b_{temp}}} \tag{13}$$

The contributors to the pyroelectric DU model noise budget include the standard deviation of the detector noise ξ_{det}, the amplifier/filter chain noise ξ_{amp}, and the ADC digitisation noise. In this case, the expression of the standard deviation of the total noise is, thus, as follows:

$$\xi_{pyr} = \sqrt{\frac{\xi_{det}^2 + \xi_{amp}^2 + \xi_{ADC}^2}{b_{spat} \times b_{temp}}} \tag{14}$$

4. Flux Incident on the Detector

4.1. Source Flux

The source spectral radiance L_s is converted into an entrance spectral flux F_E using the instrument optical etendue G:

$$F_E(\sigma) = L_s(\sigma) G \tag{15}$$

The source spectral flux incident on the detector F_s is as follows:

$$F_s(\sigma, \delta) = F_{s,DC}(\sigma) + F_{s,AC}(\sigma) cos(2\pi\sigma\delta) \tag{16}$$

where $F_{s,DC}$ the unmodulated flux and $F_{s,AC}$ the modulated flux can be expressed using F_E and the DC and AC optical transmissions of the instrument (K_{DC}, K_{AC}):

$$F_s(\sigma, \delta) = [K_{DC}(\sigma) + K_{AC}(\sigma) cos(2\pi\sigma\delta)] F_E(\sigma) \tag{17}$$

K_{DC} and K_{AC} are the products of each sub-system optical transmission K_j with $j = \{scan, FT, IA, BT, CW, filter\}$:

$$K_{DC}(\sigma) = K_{scan}(\sigma)K_{FT}(\sigma)K_{IA,DC}(\sigma)K_{BT}(\sigma)K_{CW}(\sigma)K_{filter}(\sigma) \quad (18)$$

$$K_{AC}(\sigma) = K_{scan}(\sigma)K_{FT}(\sigma)K_{IA,AC}(\sigma)K_{BT}(\sigma)K_{CW}(\sigma)K_{filter}(\sigma) \quad (19)$$

K_{DC} and K_{AC} differ in the IA unmodulated and modulated optical transmission ($K_{IA,DC}$ and $K_{IA,AC}$), respectively, which depend on the CC reflectivity R_{CC}, the BS transmission and reflectivity (K_{BS},R_{BS}), the plates absorption coefficient α_P, and the AR coating transmission K_{AR}. For the sake of clarity, we will omit the spectral dependency symbol "(σ)" in Section 4 for each transmission and reflectivity factor, only including it at the end. The expression of $K_{IA,DC}$ and $K_{IA,AC}$ are as follows:

$$K_{IA,DC}(\sigma) = R_{BS}K_{BS}\alpha_{BP}\alpha_{CP} \times \left[\alpha_{BP}^2 R_{CC1}K_{AR}^5 + \alpha_{CP}^2 R_{CC2}K_{AR}^7\right](\sigma) \quad (20)$$

$$K_{IA,\mathrm{AC}}(\sigma) = 2R_{BS}K_{BS}\alpha_{BP}^2\alpha_{CP}^2K_{AR}^6\sqrt{R_{CC1}R_{CC2}}(\sigma) \quad (21)$$

The IA reflects the back optics self-emitted flux as explained in the next section, Section 4.2, with the following reflectivity factors $R_{IA,DC}$ and $R_{IA,AC}$:

$$R_{IA,DC}(\sigma) = \alpha_{CP}^2 \times \left[K_{BS}^2\alpha_{BP}^2R_{CC1}K_{AR}^6 + R_{BS}^2\alpha_{CP}^2R_{CC2}K_{AR}^8\right](\sigma) \quad (22)$$

$$R_{IA,\mathrm{AC}}(\sigma) = 2R_{BS}K_{BS}\alpha_{CP}^2K_{AR}^7\sqrt{\alpha_{BP}^2\alpha_{CP}^2R_{CC1}R_{CC2}}(\sigma) \quad (23)$$

4.2. Thermal Background Flux

4.2.1. Unmodulated Thermal Background Flux

All the instrument sub-systems emit a DC self-emission flux directly emitted toward the detector (red arrows in Figure 5) that contribute to the background flux. Their individual expressions $F_{bg,j,DC}$ with $j = \{scan, FT, IA, BT, CW, filter\}$ are as follows:

$$F_{bg,scan,DC}(\sigma) = G\varepsilon_{scan}(\sigma)L_{BB}(T_{scan},\sigma)K_{FT}K_{IA,DC}K_{BT}K_{CW}K_{filter}(\sigma) \quad (24)$$

$$F_{bg,FT,DC}(\sigma) = G\varepsilon_{FT}(\sigma)L_{BB}(T_{FT},\sigma)K_{IA,DC}K_{BT}K_{CW}K_{filter}(\sigma) \quad (25)$$

$$F_{bg,IA,DC}(\sigma) = G\varepsilon_{IA,DC}(\sigma)L_{BB}(T_{IA},\sigma)K_{BT}K_{CW}K_{filter}(\sigma) \quad (26)$$

$$F_{bg,BT,DC}(\sigma) = G\varepsilon_{BT}(\sigma)L_{BB}(T_{BT},\sigma)\left[K_{CW}K_{filter}(\sigma) + R_{IA,DC}K_{CW}K_{filter}K_{BT}(\sigma)\right] \quad (27)$$

$$F_{bg,CW,DC}(\sigma) = G\varepsilon_{CW}(\sigma)L_{BB}(T_{CW},\sigma)\left[K_{filter}(\sigma) + R_{IA,DC}K_{CW}K_{filter}K_{BT}^2(\sigma)\right] \quad (28)$$

$$F_{bg,filter,DC}(\sigma) = \pi \mathrm{A}_{DU}\varepsilon_{filter}(\sigma)L_{BB}\left(T_{filter},\sigma\right)\left[1 + R_{IA,DC}K_{CW}^2K_{filter}K_{BT}^2(\sigma)\right] \quad (29)$$

where L_{BB} is the Planck's law radiation [2], ε the emissivity, T the temperature, and A_{DU} the studied active detection area.

Because the filter is located inside, its self-emission is integrated over the full projected half-space π [44]. Each sub-system's emissivity is calculated as one minus its transmission and reflectivity, except for the IA, which is detailed in Appendix A.

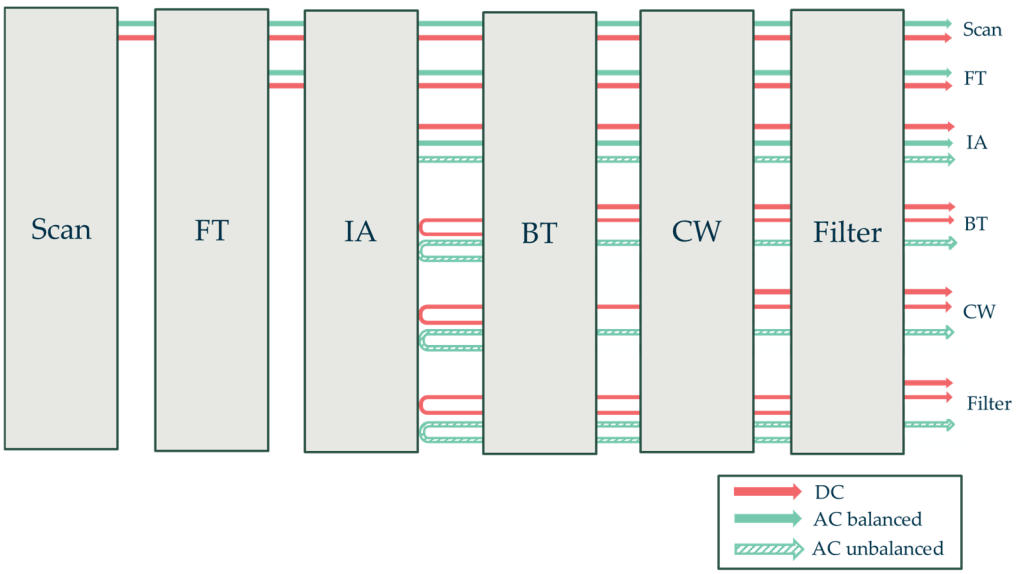

Figure 5. Layout of thermal background flux emitted from the scan mirror to the filter, with a distinction between the DC flux (red), AC balanced flux (full green), and AC unbalanced (dashed green).

4.2.2. Balanced Modulated Thermal Background Flux

The flux emitted by a component located between the entrance pupil and the IA is modulated in phase with the source flux ('balanced output' in [45]). As represented by green full arrows in Figure 5, the scan mirror, the FT, and the IA BP (see Figure A1 in Appendix A) emit a balanced background flux ($F_{bg,scan,AC}$, $F_{bg,FT,AC}$, $F_{bg,IA,AC,1}$) expressed as follows:

$$F_{bg,scan,AC}(\sigma) = G\varepsilon_{scan}(\sigma)L_{BB}(T_{scan},\sigma)K_{FT}K_{IA,AC}K_{BT}K_{CW}K_{filter}(\sigma) \quad (30)$$

$$F_{bg,FT,AC}(\sigma) = G\varepsilon_{FT}(\sigma)L_{BB}(T_{FT},\sigma)K_{IA,AC}K_{BT}K_{CW}K_{filter}(\sigma) \quad (31)$$

$$F_{bg,IA,AC,1}(\sigma) = G\varepsilon_{IA,AC,1}(\sigma)L_{BB}(T_{IA},\sigma)K_{BT}K_{CW}K_{filter}(\sigma) \quad (32)$$

4.2.3. Unbalanced Modulated Thermal Background Flux

The flux emitted by a component located between the IA and the DU is reflected by the interferometer towards the detector. It is modulated in phase opposition with the source flux ('unbalanced output' in [45]). As represented by green dashed arrows in Figure 5, the IA CP, the BT, the CW, and the filter (see Figure A1 in Appendix A) yield the following unbalanced modulated background flux incident on the detector ($F_{bg,IA,AC,2}$, $F_{bg,BT,AC}$, $F_{bg,CW,AC}$, $F_{bg,filter,AC}$):

$$F_{bg,IA,AC,2}(\sigma) = -G\varepsilon_{IA,AC,2}(\sigma)L_{BB}(T_{IA},\sigma)K_{BT}K_{CW}K_{filter}(\sigma) \quad (33)$$

$$F_{bg,BT,AC}(\sigma) = -G\varepsilon_{BT}(\sigma)L_{BB}(T_{BT},\sigma)\left[K_{CW}K_{filter}(\sigma) + R_{IA,AC}K_{CW}K_{filter}K_{BT}(\sigma)\right] \quad (34)$$

$$F_{bg,CW,AC}(\sigma) = -G\varepsilon_{CW}(\sigma)L_{BB}(T_{CW},\sigma)\left[K_{filter}(\sigma) + R_{IA,AC}K_{CW}K_{filter}K_{BT}^2(\sigma)\right] \quad (35)$$

$$F_{bg,filter,AC}(\sigma) = -\pi A_{DU}\varepsilon_{filter}L_{BB}\left(T_{filter},\sigma\right)\left[1 + R_{IA,AC}K_{CW}^2K_{filter}K_{BT}^2(\sigma)\right] \quad (36)$$

where the minus sign in the equation characterises the unbalanced modulation.

4.2.4. Detection Unit Thermal Background Flux

The detector cryostat thermal is integrated over the full half-space π, minus the source beam solid angle. The cryostat emissivity is assumed to be equal to 1 and the associated unmodulated background flux $F_{bg,DU,box}$ is as follows:

$$F_{bg,DU,box}(\sigma) = (\pi A_{DU} - G)L_{BB}(T_{DU,box}, \sigma) \tag{37}$$

A fraction of the detector's self-emission beam travels through the filter, the CW and the BT towards the IA, where it is reflected back towards the detector. The flux incident on the detector following this optical path is as follows:

$$F_{bg,DU,mat}(\sigma, \delta) = -\alpha_{DU,mat} G_E L_{BB}(T_{DU,mat}, \sigma) R_{IA,AC} K_{CW}^2 K_{filter}^2 K_{BT}^2(\sigma) \tag{38}$$

where absorption $\alpha_{DU,mat}$ is the detector material absorbance.

In the case of a photodetector located in a cryostat, the term $F_{bg,DU,mat}$ is neglected. In the case of a pyroelectric detector insensitive to the unmodulated signal, $F_{bg,DU,box}$ is not considered.

5. Instrumental Degradations and Spectral Response

5.1. Modulation Efficiency

The instrument is subject to errors associated with the quality of optics and misalignments which, consequently, diminishes the interferogram contrast [27]. We assess the associated contrast by using the modulation efficiency M:

$$M(\sigma) = M_{tilt}(\sigma) M_{shear}(\sigma) M_{WFE}(\sigma) M_{\tau_{int}}(\sigma) \tag{39}$$

where M_{tilt} is the contrast loss associated to the angular tilt between the two interfering wavefronts, M_{shear} represents the contrast loss due to the shear between these wavefronts, M_{WFE} is the contrast loss induced by the differential WFE between the two interfering waves, and $M_{\tau int}$ is associated to the signal integrated over the exposure time τ_{int}. In the model, the instrument errors are assumed to be static during the acquisition.

M_{tilt} associated with the angular tilt between the two interfering wavefronts γ_{tilt}, an aperture stop of equivalent radius R_{stop} writes, using the Bessel function of first kind J_1, as follows [27]:

$$M_{tilt}(\sigma) = \frac{2J_1(2\pi\sigma\gamma_{tilt}R_{stop})}{2\pi\sigma\gamma_{tilt}R_{stop}} \tag{40}$$

M_{shear} corresponding to the contrast loss induced by the shear γ_{shear} and a solid angle Ω writes as follows [46]:

$$M_{shear}(\sigma) = \frac{2J_1\left(2\sigma\gamma_{shear}\sqrt{\pi\Omega}\right)}{2\sigma\gamma_{shear}\sqrt{\pi\Omega}} \tag{41}$$

The contrast loss induced by the differential WFE between the two interfering waves M_{WFE} induced by the differential WFE between the two interfering waves $\Delta\delta^2$ is as follows [27]:

$$M_{WFE}(\sigma) = 1 - 2\pi^2\sigma^2\langle\Delta\delta^2\rangle \tag{42}$$

The contrast loss M_{int} associated to the signal integrated over the exposure time τ_{int}. during the dynamic CC motion at constant optical speed v_{opt} is expressed as follows [31]:

$$M_{\tau_{int}}(\sigma) = sinc(\sigma\tau_{int}v_{opt}) \tag{43}$$

5.2. Self-Apodisation and Spectral Response

Self-apodisation is due to the OPD in-field variations [28]. The output flux F of an off-axis beam propagating inside the IA with an off-axis angle θ_0 is as follows [28]:

$$F(\sigma, \delta, \theta_0) = F_{DC}(\sigma) + F_{AC}(\sigma)cos(2\pi\sigma\delta cos\theta_0) \quad (44)$$

The flux incident on the detector for a beam propagating in the angular direction angle θ_0 and of solid angle Ω is as follows [28]:

$$F(\sigma, \delta, \theta_0, \Omega) = F_{DC}(\sigma) + F_{AC}(\sigma)O_{apo}(\sigma, \delta, \theta_0, \Omega)\left\{cos\left(2\pi\sigma\delta cos\theta_0\left(1 - \frac{\Omega}{4\pi}\right)\right)\right\} \quad (45)$$

where $cos\theta_0(1 - \Omega/4\pi)$ is equivalent to a shift of the wavenumber, and O_{apo} is the term representing the self-apodisation instrument function component acting on the interferogram contrast [27].

It is important to mention that O_{apo} depends both on the wavenumber and the OPD and that the impact of the self-apodisation on the contrast is maximum at σ_{max}. In the model, we therefore decided to compute the instrument function at σ_{max}.

The other contributor to the instrument function is the restriction on the OPD range due to the restricted displacement range of the dynamic CC. The signal is acquired between −MOPD and +MOPD where MOPD is the maximum optical path difference. The associated contributor O_{range} to the instrument function is represented as a unit boxcar function [28]:

$$O_{range}(\delta) = \prod\left(\frac{\delta}{2MOPD}\right) \quad (46)$$

The global instrument function is as follows:

$$O(\delta) = O_{range}(\delta) \times O_{apo}(\delta) \quad (47)$$

The spectral response, named the instrument line shape (ILS), is defined as the real Fourier transform of the instrument function.

$$ILS(\sigma) = \Re[FT\{O(\delta)\}] \quad (48)$$

The resolution-limited spectrum measured by the instrument is therefore the convolution of the entrance spectrum with the ILS. In this paper, the spectral resolution is defined as the ILS central lobe full width at half maximum (FWHM). Figure 6 represents the focal plane (left panel) and the ILS (right panel) of the GLORIA instrument at σ = 1400 cm^{-1}, an MOPD of 8 cm, an FOV of 26.6 × 70.9 mrad^2, and a pixel FOV of 0.56 × 0.56 mrad^2 [11]. On the right panel, we estimate that the on-axis ILS FHWM is equal to 0.0753 cm^{-1} while its FWHM increases to 0.0764 cm^{-1} for the beam propagating at the top left corner pixel of angular coordinate (13.3 mrad; 35.4 mrad). In this figure, we notice that the relative spectral shift of the wavenumber $cos\theta_0(1 - \Omega/4\pi)$ equals 0.9993, which displaces the line at σ = 1400 cm^{-1} to σ = 1399.016 cm^{-1}.

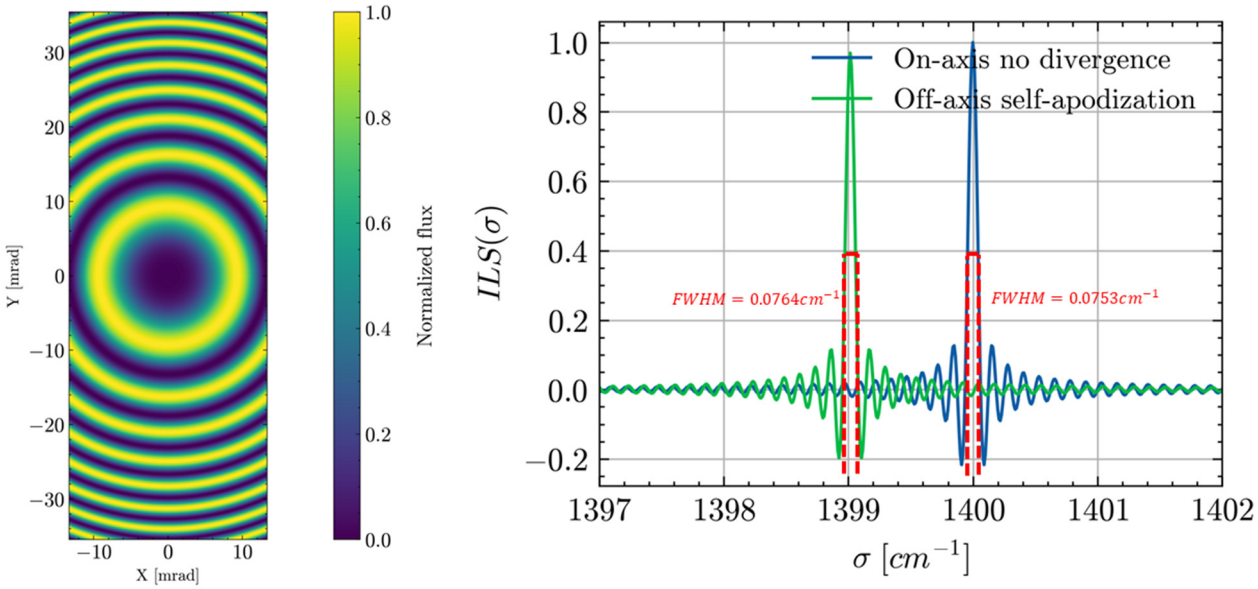

Figure 6. Effect of self-apodisation on GLORIA at σ = 1400 cm^{-1} on focal plane irradiance distribution of angular dimension equal to 70.9 × 26.6 mrad^2 at 8 cm MOPD (**left panel**) and the spectral response at a pixel of coordinate (13.3 mrad; 35.4 mrad) (**right panel**).

6. Radiometric Performance Budget

In this section, we calculate two common metrics to estimate the radiometric performance: the Noise-Equivalent Spectral Radiance (NESR) and the Noise-Equivalent Differential Temperature (NEDT).

The NESR [27] is calculated by first converting the interferogram noise standard deviation ξ to the domain of the signal Fourier transform ξ_σ [47].

$$\xi_\sigma = \frac{1}{d\sigma}\sqrt{\frac{2}{M_{ifg}}}\xi \tag{49}$$

where M_{ifg} is the interferogram number of samples and $d\sigma$ the spectral sampling. Depending on the DU type, the NESR is calculated as follows:

$$NESR_{ph}(\sigma) = \frac{\xi_\sigma}{\frac{1}{hc\sigma}K_{AC}(\sigma)G\eta(\sigma)\tau_{int}M(\sigma)\rho} \tag{50}$$

$$NESR_{pyro}(\sigma) = \frac{\xi_\sigma}{\frac{1}{hc\sigma}K_{AC}(\sigma)G\alpha_{pyro}(\sigma)R_V(\sigma)M(\sigma)} \tag{51}$$

The NEDT is computed for a temperature T_s scene using Planck's law temperature derivative [48]:

$$NEDT(\sigma) = \frac{NESR(\sigma)}{\left[\frac{\partial L_{BB}(\sigma,T)}{\partial T}\right]_{T_s}} \tag{52}$$

7. Inverse Model

7.1. Inverse Model Overview

The inverse model (Figures 7 and 8) reconstructs a spectrum from two input calibrations and one input science interferograms provided by the instrument model as it is usually carried out in a L1 ground processor [49]. The outputs of the inverse model are the scene spectral radiance, the instrument radiometric gain, and the radiometric offset, including their respective noises. The reconstruction process comprises four analytical

steps described hereafter. First, we compute the Fourier transform of the three input interferograms according to Equation (53) in Section 7.2. Second, we estimate the radiometric gain and offset from the Fourier transform of the interferograms of the two calibration sources (dark and bright) and the known spectral radiance of these sources, as described in Section 7.2 by Equations (55) and (56). Third, we reconstruct the scene spectrum from the Fourier transform of the science interferogram by using the radiometric gain and offset according to Equation (54) in Section 7.2. Finally, the model propagates the noise in the reconstruction process as detailed later in Section 7.3.

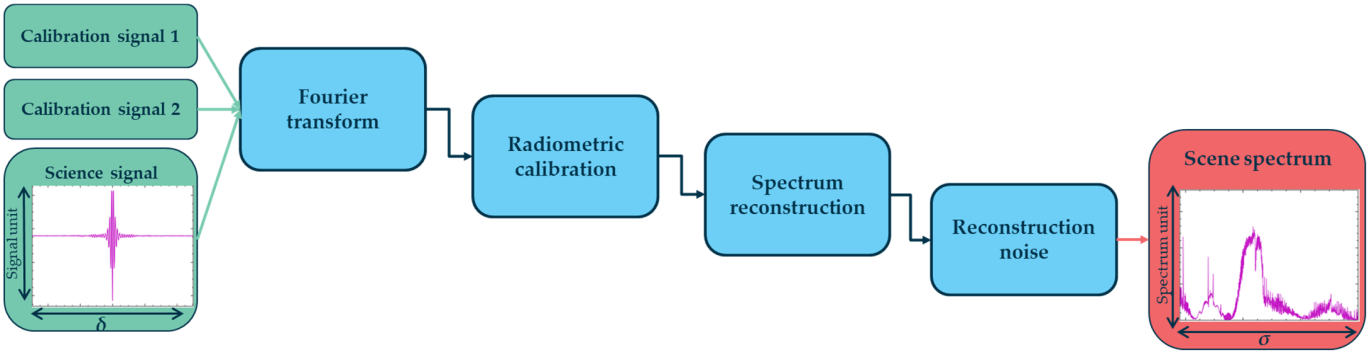

Figure 7. Inverse model architecture with the inputs filled in green, the outputs filled in red and the inverse model parts in blue.

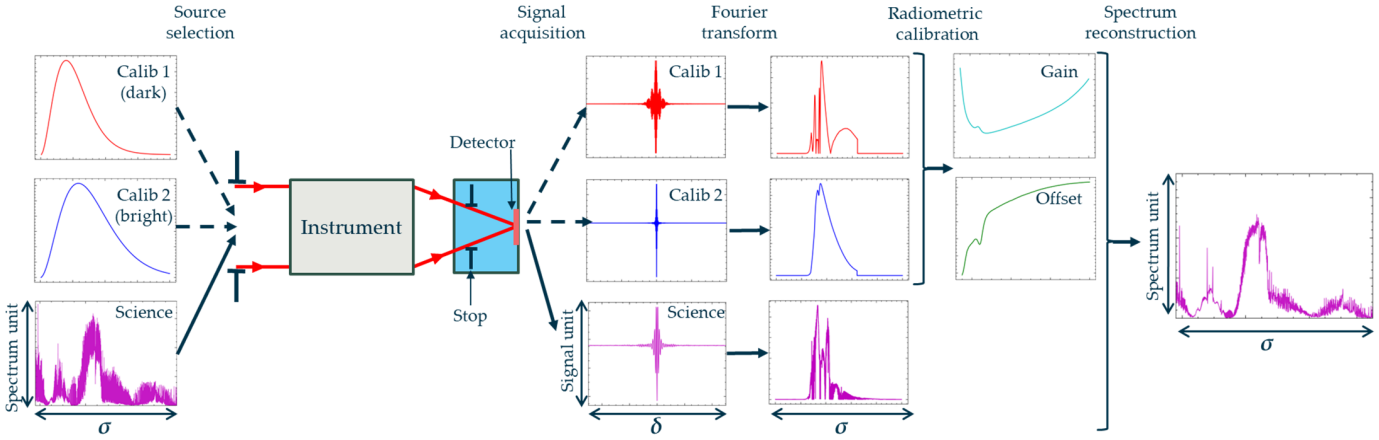

Figure 8. Radiometric calibration and science spectrum reconstruction scheme. The dark (red) and bright (blue) calibration sources, labelled "Calib" and selected with dashed arrows on the figure, have known spectral radiance used in the radiometric calibration step to estimate the instrument gain and offset.

7.2. Radiometric Calibration and Spectrum Reconstruction

The instrument model provides a modulated signal N_{AC}. We offer the option to zero-fill the signal, which interpolates the reconstructed spectrum and speeds up the Fast Fourier Transform algorithm if the number of points after filling corresponds to the next power of two [2]. We also include the possibility to perform a numerical apodisation of the signal to mitigate the "ringing" phenomenon [2]. The complex signal in the spectrum domain N_σ is the Fourier transform of the modulated signal.

$$N_\sigma(\sigma) = FT\{N_{AC}(\delta)\} \tag{53}$$

The relation between N_σ, the entrance spectral radiance L, the instrument complex radiometric gain G, and offset L_0 is as follows [26]:

$$L(\sigma) = \Re\{N_\sigma(\sigma)G(\sigma) - L_0(\sigma)\} \tag{54}$$

Since the relation between N_σ and L is linear, the gain and the offset are estimated from the acquisition of two calibration sources (1,2) with known spectral radiances (L_1,L_2) associated with two complex signals ($N_{\sigma,1}$,$N_{\sigma,2}$):

$$G(\sigma) = \frac{L_1(\sigma) - L_2(\sigma)}{N_{\sigma,1}(\sigma) - N_{\sigma,2}(\sigma)} \tag{55}$$

and

$$L_0(\sigma) = N_{\sigma,2}(\sigma)G(\sigma) - L_2(\sigma) \tag{56}$$

The spectral variability of G is induced by the optical transmission of the instrument, the response of the detector, and the modulation loss. The offset radiance L_0 is caused by the modulated self-emission of the instrument. It is important to note that, in our definition, G is expressed as spectral radiance per signal unit. Other similar methods define the gain as signal per signal unit, which means they divide $N\sigma$ by G rather than multiplying in Equations (54) and (56).

There are no principal limitations to the wavenumber range of a two-point calibration, if the "bright" calibration source does not saturate the pixels. Additionally, the radiometric gain and offset noise should stay relatively low compared to G and L_0. To achieve this last condition, it is possible to increase the number of averaged calibration source measurements.

7.3. Noise Propagation in Spectrum Reconstruction

In addition to a numerical propagation of the interferogram noise to the spectrum, we also analytically assess this propagation in the reconstruction equations. To estimate the spectrum noise standard deviation ξ_L, we start from inserting Equations (55) and (56) into (54) to obtain an explicit expression of the reconstructed spectral radiance L_s as a function of the calibration and scene signals:

$$L_s(\sigma) = \Re\left\{\frac{L_1(\sigma) - L_2(\sigma)}{N_{\sigma,1}(\sigma) - N_{\sigma,2}(\sigma)}(N_{\sigma,s}(\sigma) - N_{\sigma,2}(\sigma)) + L_2(\sigma)\right\} \tag{57}$$

The noise between distinct signal acquisitions is assumed to be uncorrelated and the propagation of both the calibration and scene signal noise can be expressed accordingly:

$$\xi_L(\sigma) = \sqrt{\xi_{\sigma,s}^2\left|\frac{\partial L_s(\sigma)}{\partial N_{\sigma,s}(\sigma)}\right|^2 + \xi_{\sigma,1}^2\left|\frac{\partial L_s(\sigma)}{\partial N_{\sigma,1}(\sigma)}\right|^2 + \xi_{\sigma,2}^2\left|\frac{\partial L_s(\sigma)}{\partial N_{\sigma,2}(\sigma)}\right|^2} \tag{58}$$

thus yielding

$$\xi_L(\sigma) = \sqrt{\xi_{\sigma,s}^2|G(\sigma)|^2 + \xi_{\sigma,1}^2|G(\sigma)|^2\left(\frac{L_s(\sigma) - L_2(\sigma)}{L_1(\sigma) - L_2(\sigma)}\right)^2 + \xi_{\sigma,2}^2|G(\sigma)|^2\left(\frac{L_s(\sigma) - L_1(\sigma)}{L_1(\sigma) - L_2(\sigma)}\right)^2} \tag{59}$$

Finally, considering the following relation between G, ξ_σ and the NESR [50],

$$NESR(\sigma) = |G(\sigma)|\xi_\sigma \tag{60}$$

we deduce that

$$\xi_L(\sigma) = \sqrt{NESR_s^2(\sigma) + \left[NESR_1(\sigma)\left(\frac{L_s(\sigma) - L_2(\sigma)}{L_1(\sigma) - L_2(\sigma)}\right)\right]^2 + \left[NESR_2(\sigma)\left(\frac{L_s(\sigma) - L_1(\sigma)}{L_1(\sigma) - L_2(\sigma)}\right)\right]^2} \quad (61)$$

This last formulation highlights the relation between the instrument's radiometric performance (NESR), the dynamics between the different calibration and scientific source spectral radiances, and the reconstructed spectrum noise standard deviation. Equation (59) can also be written in terms of noise temperature using Equation (50). It is important to notice that the numerical apodisation of the interferogram is not included in this consideration.

This method enables an evaluation of both the instrument's radiometric performance and the calibration strategy regarding their effects on the quality of the reconstructed scene's spectral radiance. It is important to notice this section exclusively details the analysis of the reconstructed spectrum noise propagation while the model also evaluates the noise on the gain and the offset (see Appendix B).

8. Instrument Model Validation

8.1. The GLORIA-Lite Instrument

GLORIA-Lite (Figure 9 and Table 3) is an atmospheric limb emission sounder built and operated by the Karlsruher Institut für Technologie (KIT) and the Forschungszentrum Jülich (FZJ). It has crossed the Atlantic on a stratospheric balloon in June 2024 and delivered several terabytes of limb emission spectra during this mission [51]. GLORIA-Lite is a double pendulum interferometer with fixed plane retroreflectors. The interferometer uses a diamond beamsplitter without any compensation plate. The moving mirrors are two CCs mounted on a rotating structure and provide an MOPD of 25 mm. The back optics is a fully reflective design with an effective focal length of 60 mm. The operation temperature is ambient, which means that the instrument drifts thermally in the range from 20 °C to −20 °C during the balloon flight. The detector system is a mercury cadmium telluride (MCT) large-focal-plane array (LFPA) with a 15 µm pitch operating at 75 K and covers the thermal infrared spectral region. A 2 × 2 hardware binning and a 1 × 48 software binning are used to achieve a spatial sampling of 300 m × 14 km at the horizon. Two calibration sources, a blackbody that is radiatively cooled, and deep space are used for the determination of the radiometric offset and gain. The structure of the blackbody deployed on GLORIA-Lite is very close to the one used for GLORIA which has been characterised at Physikalisch-Technische Bundesanstalt (PTB), the national metrology institute of Germany [52]. A similar characterisation of the GLORIA-Lite blackbody at PTB is planned. The pyramidal structure of the baseplate is very close to the one used for GLORIA, the coating is identical, and the same type of aged and calibrated temperature sensors are used. Therefore, similar values of emissivity and radiometric accuracy are expected.

Table 3. GLORIA-Lite essential properties.

Property	Value
Mass	35 kg
Power consumption	80 W
Spatial sampling at horizon	300 m × 14 km
Spectral sampling	0.2 cm^{-1}
Spectral coverage	750–1390 cm^{-1}
Sensitivity	~10 $nW/(cm^2\ sr\ cm^{-1})$

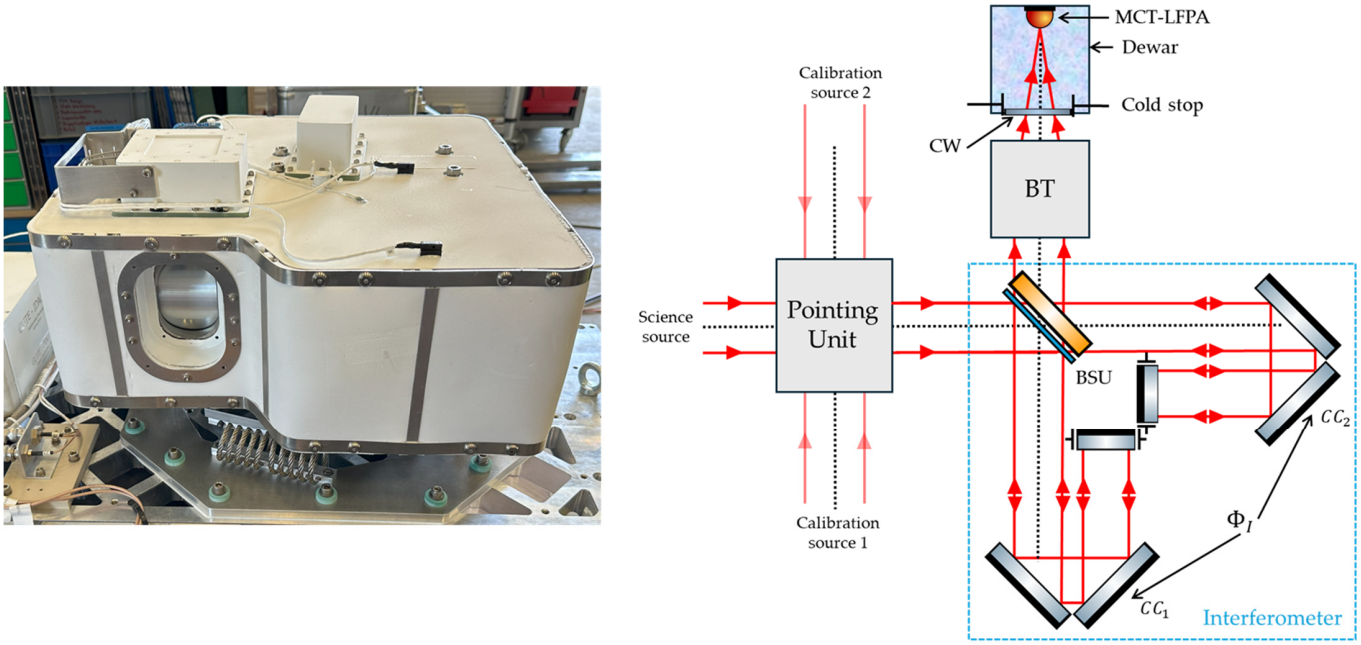

Figure 9. GLORIA-Lite spectrometer. (**Left panel**) Instrument during its integration phase in Kiruna in 2024. (**Right panel**) Instrument model setup of GLORIA-Lite. This sketch was created using the Component Library by Alexander Franzen, licensed under CC BY-NC 3.0.

8.2. Validation with GLORIA-Lite In-Flight Signals

In this section, we present an analysis of GLORIA-Lite signal measurements consisting of Level 0 processed in-flight data [49] that we compare to the model predictions. All this is carried out while observing a 241.316 K blackbody and the deep space. These measurements were taken at a 39.3 km balloon flight altitude. It is important to mention that GLORIA-Lite is a balloon-borne embedded instrument located at an altitude where the so-called "deep space source" is not very "deep", and some atmospheric residuals are included into these measurements [53]. KIT has measured and provided this additional emission such that, in the model, the spectral radiance of the deep space source corresponds to the one measured by GLORIA. This measurement with the associated viewing geometry is presented in Figure 10. We implemented the GLORIA-Lite layout into the model by inputting the instrumental parameters provided by KIT and described in Section 8.1.

For each GLORIA-Lite detector pixel, the in-flight DC level is computed as the average of the first and last 2000 frames signal, which corresponds to an OPD range of 0.4 cm as represented in Figure 11. We noticed that the difference in the DC levels between the first and last frame calculation is negligible (<0.1%), and we thus decided to show the figures related to the first 2000 frames only.

On the deep space acquisition, the model predicts 7.07 Me^{-} for the baseline and 7.86 Me^{-} for the ZPD levels, with atmospheric residuals and dark current accounting for about 0.6% and 5% of the total DC photonic level, respectively (Figure 12). The instrument self-emission represents here more than 94% of the total signal, thus constituting the major contributor.

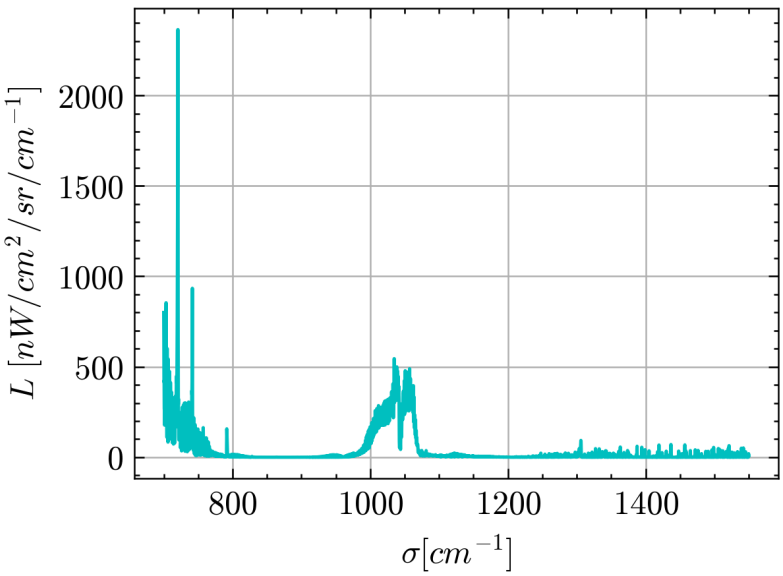

Figure 10. Residual atmospheric spectrum measured during a deep space acquisition at a 39.3 km balloon flight altitude, pointing at a 20° pitch elevation angle. The associated GPS coordinates are 67.59° latitude and 17.87° longitude.

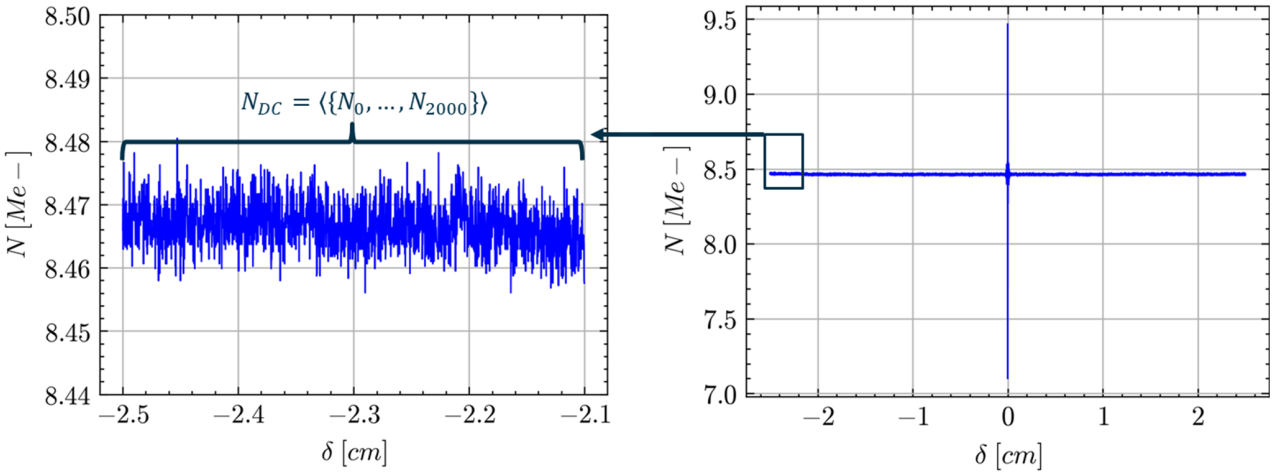

Figure 11. Illustration of the baseline signal estimation as the average first 2000 frames signal indicated by the dark box and arrow.

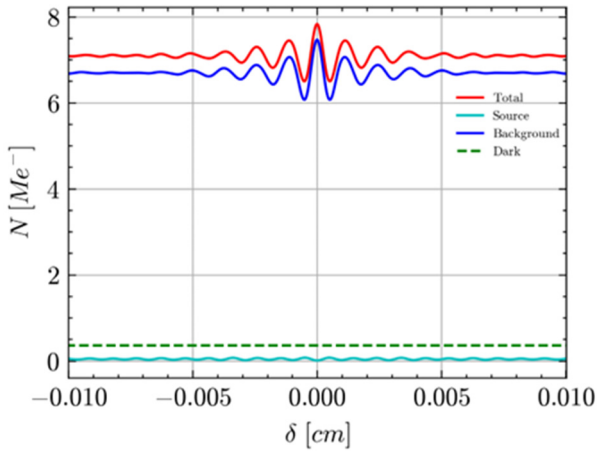

Figure 12. Contribution of the dark current (dashed green), the atmospheric residuals (cyan), and the instrument thermal background (blue) to the predicted total signal of a deep space acquisition.

We represent in Figure 13's left panel the signal of a deep space acquisition obtained by the model (red) and measured during GLORIA-Lite flight (blue), at the central pixel. Figure 13's middle and right panels, respectively, show the histograms of DC and ZPD signal measurements over the whole detector, versus the level predicted by the model (red dashed line). The measured baseline and ZPD levels are 7.15 $\pm$ 0.16 Me^- and 7.86 $\pm$ 0.16 Me^-, respectively. The model predictions thus lie in the range of these measurements. The standard deviation of the signal histogram represents between 2% and 2.5% of the average signal that corresponds to a typical level of detector PRNU [54]. The agreement between the predicted and measured average signals validates the ability of the model to predict the signal dynamic of a "deep sky source".

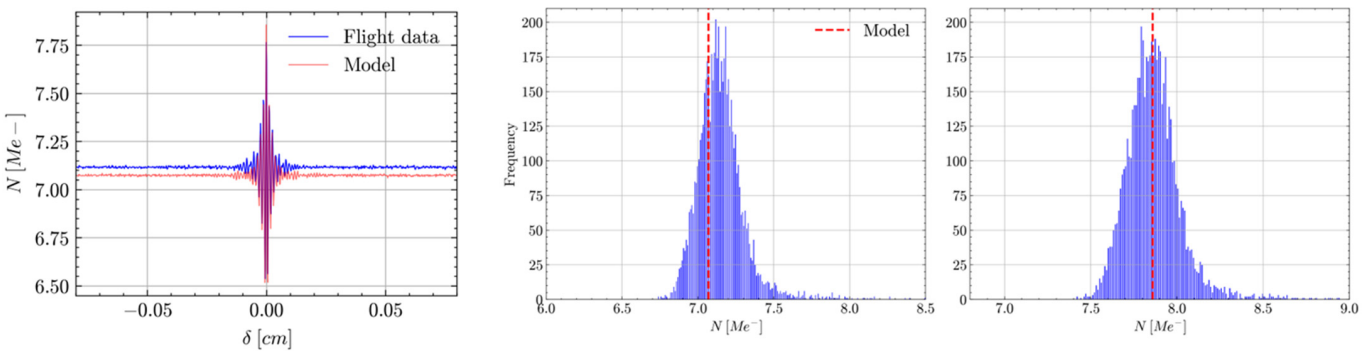

Figure 13. Model predictions (red) and in-flight measurements (blue) of GLORIA-Lite deep space signals. (**Left panel**) Central pixel signal. (**Centre panel**) Histogram of GLORIA DC level over the detector. (**Right panel**) Histogram of GLORIA ZPD level over the detector.

We performed the same analysis on the signal acquisition of a 241.316 K blackbody (Figure 14). Looking at the DC and ZPD signals over the detector (middle and right panels), the measured baseline and ZPD level are 8.50 $\pm$ 0.16 Me^- and 7.11 $\pm$ 0.15 Me^-, respectively. The model predicts a baseline level of 8.61 Me^- and a ZPD level of 7.14 Me^-. As for the deep space view, the model predictions are in good agreement with the measurements. This validates the model capability to predict the signal dynamic of a blackbody calibration source.

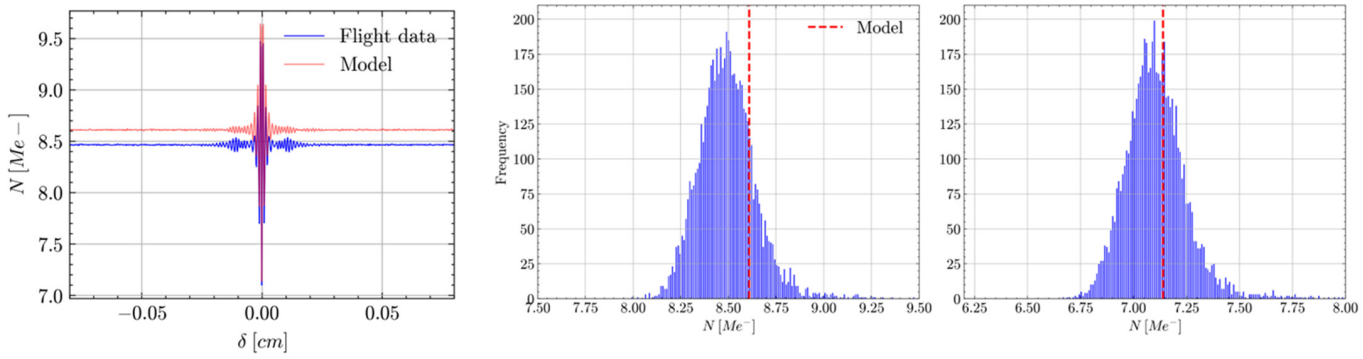

Figure 14. Model predictions (red) and in-flight measurements (blue) of GLORIA-Lite blackbody signals. (**Left panel**) Central pixel signal. (**Centre panel**) Histogram of GLORIA DC level over the detector. (**Right panel**) Histogram of GLORIA ZPD level over the detector.

We conclude that the model can successfully predict the DC and ZPD signal levels of two calibration sources: deep space, including atmospheric residuals, and a 241.316 K blackbody. The maximum observed relative difference between the prediction and the

average signal measurements dN is only 1.3% on the blackbody baseline level, with dN defined as follows:

$$dN = \left| \frac{N_{model} - \langle N \rangle_{meas}}{\langle N \rangle_{meas}} \right| \times 100\% \quad (62)$$

where N_{model} and N_{meas} are the predicted and measured signal, respectively. We attribute these differences to the following:

1. The error on the temperature of the elements located between the scan mirror to the CW, which is estimated to be equal to 0.5 K.
2. The error on the dark current density associated with the in-flight detector measured temperature uncertainty of 0.03 K. The consequent dark current drift is deduced from the "Rule07" associated to MCT infrared photodetectors [55] and is equal to 2.16 mA/m^2.
3. The detector PRNU, which we assume to be equal to 2%.
4. The error on the blackbody emissivity, which is estimated to be equal to 0.003 based on the GLORIA calibration source stability requirement [52].
5. The error on the blackbody temperature, which is estimated to be equal to 0.03 K based on the in-flight temperature measurements precision.
6. The error on the mirrors coating reflectivity, which is estimated to be equal to 0.0005. There is one mirror in the front optics, seven per CC assembly, and four in the back optics.
7. The error on the BS substrate transmission, which is estimated to be equal to 0.005.
8. The error on the BP thickness, which is estimated to be equal to 0.05 mm.
9. The error on the BP AR coating reflectivity, which is estimated to be equal to 0.0005.

We performed an error analysis on this set of uncertainties to estimate their influence on the error of the blackbody signal estimation. We assume the listed errors to be uncorrelated. The total signal error ΔN is the quadratic sum of each contributor ΔN_i related to a parameter u_i:

$$\Delta N_i = \Delta u_i \frac{\partial N}{\partial u_i} \quad (63)$$

$$\Delta N = \sqrt{\sum_i \Delta N_i^2} \quad (64)$$

where Δu_i is the uncertainty or error associated with a signal error ΔN_i.

Table 4 presents the estimated error budget. The largest contributors of the baseline error ΔN_{DC} are the PRNU, the optics temperature, and the mirrors reflectivity that contribute to 1.95%, 0.67%, and 0.64% of the error made on the DC signal, respectively. Furthermore, the instrument thermal background dominates the radiometric budget as it represents about 68% of the total DC signal. It is thus expected that minor changes in the transmission of optics and temperature have a significant influence on the predicted signal measurements. The errors on the blackbody emissivity, the IA plate AR coating reflectivity, and the plate size, contributing to 0.17%, 0.16%, and 0.14%, respectively, are of the secondary order compared to the first three contributors. The contributions of the BS transmission, the dark current, and the blackbody temperature are considered as fully negligible. The total error represents 2.16% (0.19 Me^-) and 2.37% (0.17 Me^-) of the model baseline and ZPD signals, respectively. These results are in good agreement with the standard deviation of the measured signal distribution.

Table 4. Error budget on the baseline and ZPD signals on a blackbody acquisition.

Contributors	$\Delta N_{DC}/N_{DC}$ %	$\Delta N_{ZPD}/N_{ZPD}$ %	**Precision**
Optics temperature	0.67%	0.90%	0.5 K
Dark current	0.02%	0.03%	2.16 mA/m^2
PRNU	1.95%	1.94%	2%
Blackbody emissivity	0.09%	0.17%	0.003
Blackbody temperature	0.02%	<0.01%	0.03 K
Mirror reflectivity	0.64%	1.00%	0.0005
BS transmission	<0.01%	0.01%	0.005
BP optical thickness	0.05%	0.14%	0.05 mm
BP AR coating reflectivity	0.21%	0.16%	0.0005
Total	2.17%	2.37%	-

9. Radiometric Calibration Model Validation

In this section, we validate the radiometric calibration model by comparing the radiometric gain and offset predictions and measurements. Contrary to the acquisitions presented in Section 8, the signals are here normalised to a similar integration time of 100 µs. Atmospheric residuals of the deep space signal are already corrected in the GLORIA-Lite measurements as part of the L1 data processing [53]. For this comparison, we thus did not include these residuals in the simulated deep space acquisition.

Figure 15 represents the instrument radiometric absolute gain (left panel) and offset real part (right panel) predicted by the model, compared to the measurements between 780 cm^{-1} and 1400 cm^{-1}. The gain is low in this range where the GLORIA-Lite optics transmission and detector response are optimised. The offset is negative because most of the instrument thermal self-emission comes from the back optics and the CW.

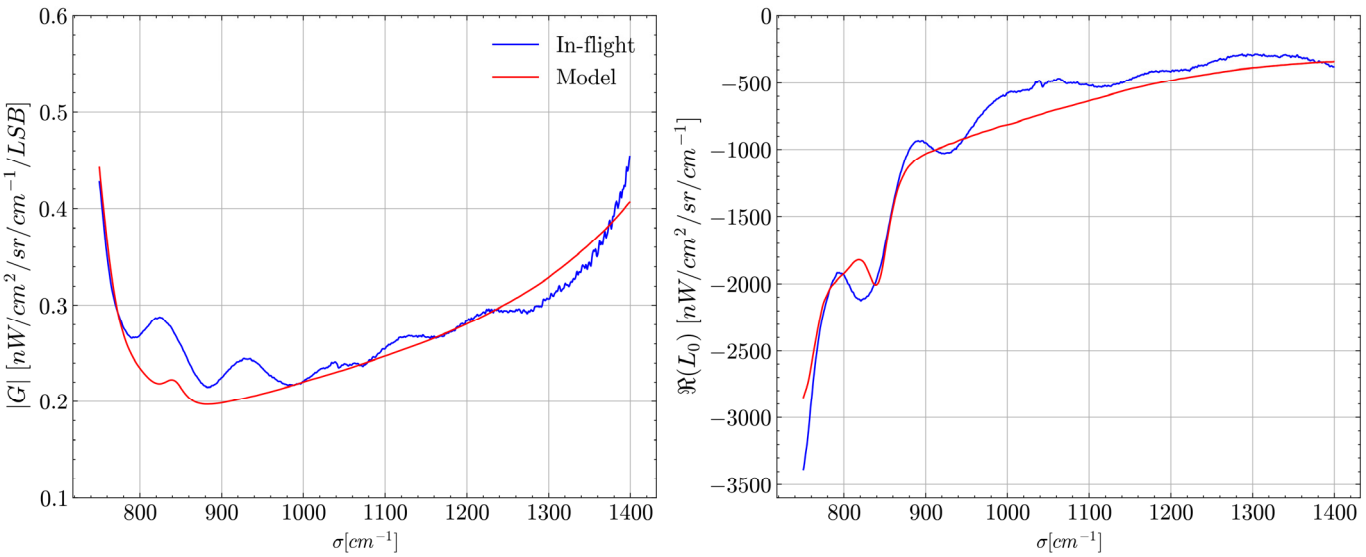

Figure 15. Model prediction (red) and in-flight measurements (blue) of GLORIA-Lite radiometric calibration outputs at the central pixel. (**Left panel**) Gain magnitude. (**Right panel**) Offset real part.

We see a good agreement between the predictions and the measurements, which shows a good knowledge of the optics and detector response, as well as the instrument temperatures. For the gain, the biggest difference between the model predictions and the measurements is located between 800 cm^{-1} and 1000 cm^{-1}, where measurements values are between 10% and 25% higher. We attribute this to an overestimation of the material and AR coating transmission from the CW and the IA plate. The input transmission curves

for these two components are based on their material bulk absorption and thickness but not on independent measurements performed on the instrument.

We also notice fluctuations between 800 cm^{-1} and 1300 cm^{-1} with an approximate period of 100 cm^{-1}. We attribute these fluctuations to the Fabry–Perot channelling effect occurring in the detector substrate [56,57]. Let us assume this substrate has a thickness d and a refractive index n. The optical path difference between a nominal beam normal to a surface which is directly transmitted and a secondary beam that is reflected twice before equals $2nd$. This corresponds in the spectrum domain to a beating frequency of $\Delta\sigma = 1/2nd$. We assume that the HgCdTe detector substrate has a refractive index of approximately 3.3 [58]. For such detectors optimised for very long-wave infrared (VLWIR), we estimate that the substrate thickness is equal to 15 µm [55]. This results in $\Delta\sigma \approx 100$ cm^{-1}, which agrees with the observed gain oscillations frequency as represented in Figure 15's left panel. The other refractive surfaces such as the IA plate and the CW are wedged to avoid this effect.

Looking at the offset, we predict up to 20% lower L_0 absolute values compared to measurements between 800 cm^{-1} and 850 cm^{-1}, likely because of the underestimation of the CW transmission. This is in accordance with the higher gain measurements in this region. The fluctuations in offset measurements between 950 cm^{-1} and 1300 cm^{-1} agree with the fluctuations observed in the gain in this range. In this region, we slightly overestimate L_0 probably due to the underestimation of the IA plate transmission. Such fluctuations in optics transmission are usually not considered in feasibility studies where manufacturing and testing have not started yet. We thus conclude that the model can predict the instrument's radiometric response and offset.

10. FTS Model Consistency Assessment

In this last section, we use both the instrument and inverse models to reconstruct a limb reference spectrum in the GLORIA-Lite spectral range. This final study serves as a consistency assessment of the entire FTS model chain's ability to accurately reconstruct a scientific spectrum. Such reconstruction is feasible only after a thorough validation of both the instrument and radiometric calibration models. Additionally, we confirm that the comprehensive model produces an output spectrum consistent with expectations when the input spectrum is convoluted with the instrument's spectral response. The reference scene is a 20 km altitude, mid-latitude day limb reference spectrum [59]. For the radiometric calibration, we simulated the averaging of 10 acquisitions of both deep space and blackbody. We also co-added the 48 pixels in the horizontal direction to mitigate noise as performed on the previous balloon-borne version of GLORIA [60].

The "original" spectrum has a 0.05 cm^{-1} spectral resolution while the instrumental resolution is 0.385 cm^{-1} after the application of a Norton–Beer strong apodisation [61]. To accelerate the Fast Fourier Transform algorithm and smooth the produced spectrum, a zero-filling up to 2^{18} points has been applied on both the calibration and the scientific source interferograms.

An illustration of the reconstruction is presented in Figure 16. The spectrum across the full spectral range is represented in the top left panel, while zoomed views over 10 cm^{-1} ranges are displayed on the other panels.

In the bottom left panel, we notice that the model can reconstruct emissions lines characteristics of Sulphur Hexafluoride (SF6) around 950 cm^{-1}. The top right panel includes a retrieval region of Ozone (O3), while the bottom right panel represents a retrieval region of the Sulphur Dioxide (SO2). The observation of these three atmospheric gases is targeted by the EE11 CAIRT candidate [9].

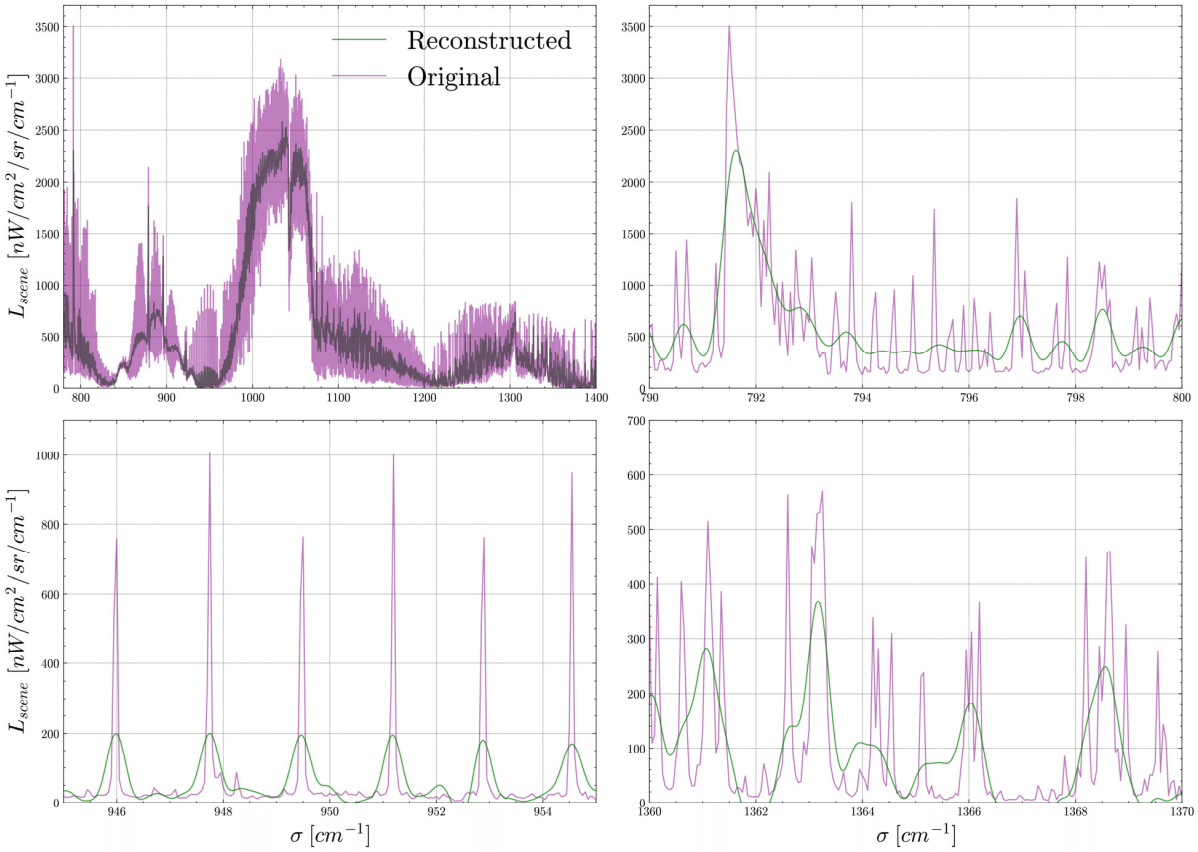

Figure 16. Limb reference scene reconstruction at 0.385 cm^{-1} apodised resolution (green) versus the "original" spectrum at 0.050 cm^{-1} resolution (magenta). A zero-filling up to 2^{18} points and a Norton–Beer strong apodisation have been applied on the interferograms. (**Top-left panel**) Global view from 780 cm^{-1} to 1400 cm^{-1}. (**Top-right panel**) Zoomed view between 790 cm^{-1} and 800 cm^{-1}. (**Bottom left panel**) Zoomed view between 945 cm^{-1} and 955 cm^{-1}. (**Bottom right panel**) Zoomed view between 1360 cm^{-1} and 1370 cm^{-1}.

In a second time, we compare the model-reconstructed spectrum with a theoretical spectrum corresponding to the instrument's apodised spectral resolution. As represented on Figure 17, this theoretical spectrum is the convolution of the "original" spectrum with the ILS considering a Norton–Beer strong apodisation. On Figure 18, this spectrum is compared with the noiseless spectral radiance from the model, examining the same three spectral ranges as presented in Figure 16. We observe that both the theoretical (red dashed lines) and the inverse model (green lines) spectral lines match. This agreement confirms the capability of the model to simulate the retrieval of a scientific source spectrum considering the instrument's spectral response and radiometric calibration.

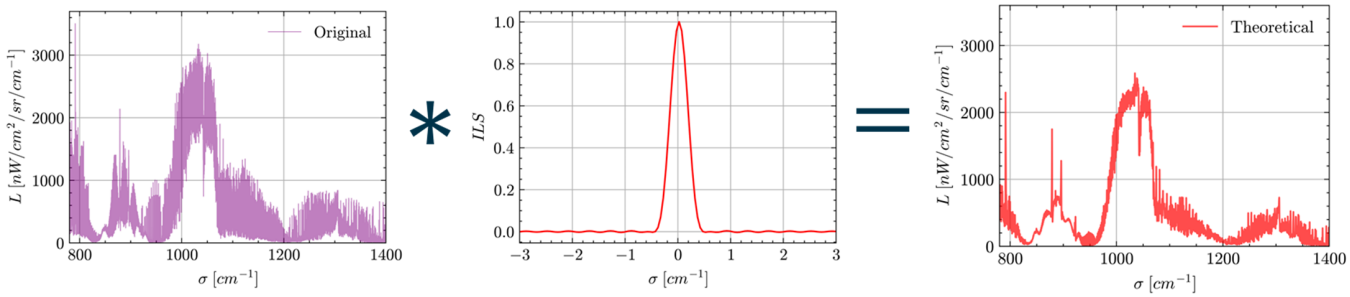

Figure 17. Theoretical spectrum (**right panel**) obtained as the convolution (* symbol) of the "original" spectrum (**left panel**) with the ILS (**middle panel**), considering a Norton–Beer strong apodisation.

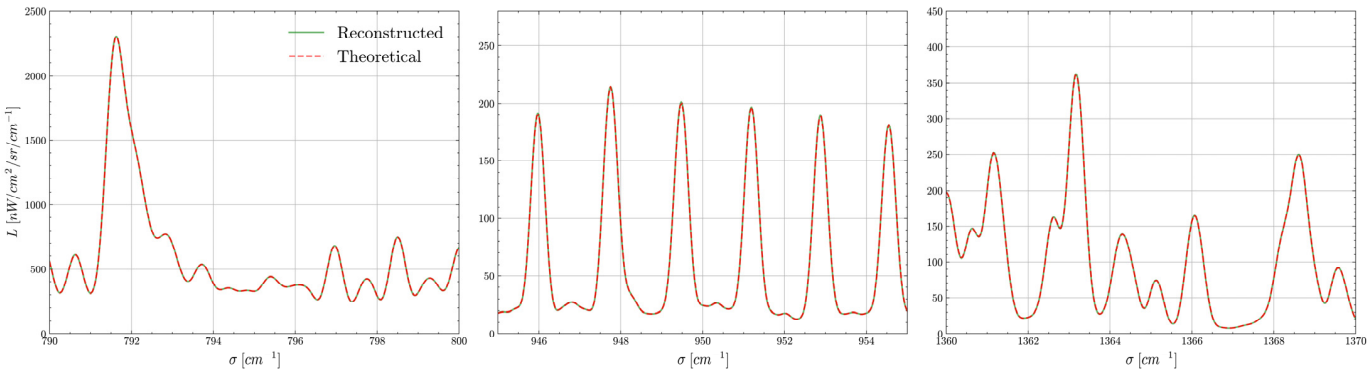

Figure 18. Comparison between the inverse model (green) and the theoretical (dashed red) noiseless spectral radiances at 0.385 cm^{-1} apodised resolution. The theoretical spectrum is obtained by the convolution of the input spectrum with the ILS and considering a Norton–Beer strong apodisation. (**Left panel**) View between 790 cm^{-1} and 800 cm^{-1}. (**Middle panel**) View between 945 cm^{-1} and 955 cm^{-1}. (**Right panel**) View between 1360 cm^{-1} and 1370 cm^{-1}.

11. Conclusions and Discussion

We have developed at ESA an FTS radiometric model to support future EO missions in phase 0/A. It is divided into an instrument and an inverse model, both described in this paper. Based on a versatile beam splitting unit model and two different types of detectors, the instrument model simulates noisy digitised interferograms from both input calibration and scientific sources. The retrieval model simulates the instrument radiometric calibration, reconstructs the scene spectral radiance, and propagates the signals noise in the process.

The ESA model and the corresponding code, with a running time in the order of 10 s only, are designed to be adaptable to various instrumental parameters. This allowed us to simulate the design of various mission payloads such as CAIRT, NITROSAT, GLORIA-B, and GLORIA-Lite which has been used for the model validation. The comparison between the model signal predictions and actual in-flight measurements indicated a maximum deviation of less than 2% for both the baseline and ZPD levels relative to the average measured levels. We are also able to predict with a good precision the instrument radiometric gain and offset, considering the uncertainties on the instrument parameters. This validates the capability of the model to accurately estimate the instrument's radiometric performance in phase 0/A. A reconstruction of a reference limb spectrum showed the ability of the model to retrieve spectral lines targeted by future EO missions monitoring atmospheric gas concentration.

The validation study indicated significant variability in the in-flight signal measurements due to the detector PRNU which has not yet been included in the model. Additionally, uncertainties regarding parameters such as optics transmission and temperature were identified. We consider implementing such parameter statistics feasible within the model and code architecture. Future versions aim to incorporate dynamic interferometer errors related to the interferometer shear, tilt, WFE, and CC displacement. Finally, we aim to extend the interferometer model to allow the simulation of a four-port configuration such as FORUM [62].

Author Contributions: Conceptualisation, methodology, validation, formal analysis, and visualisation, T.P. and C.B.; software, T.P.; investigation, T.P., C.B., F.F.-V. and A.K.; resources, F.F.-V. and A.K.; writing—original draft preparation, T.P., C.B., F.F.-V. and A.K.; writing—review and editing, T.P., C.B., F.F.-V., A.K., A.H., J.H., L.B., M.D.M., T.G., D.L., F.M., F.V. and B.V.; supervision, project administration, and funding acquisition, C.B. and A.H. All authors have read and agreed to the published version of the manuscript.

Funding: This research received no external funding.

Data Availability Statement: The datasets presented in this article are not readily available due to the inclusion of sensitive information related to proprietary industrial technologies. Requests to access the datasets should be directed to the corresponding author.

Acknowledgments: The authors thank Alizée Malavart, Alex Hoffman, and Jonathan Flunger for initiating contact regarding GLORIA. The authors would like to thank the reviewers for their valuable comments and suggestions, which have greatly contributed to improving the quality and clarity of this manuscript.

Conflicts of Interest: Author Ljubiša Babić was employed by the company Aurora Technology B.V. The remaining authors declare that the research was conducted in the absence of any commercial or financial relationships that could be construed as a potential conflict of interest.

Abbreviations and Symbols

The following abbreviations and symbols are used in this manuscript:

FTS	Fourier Transform Spectrometer
EO	Earth Observation
ESA	European Space Agency
MIPAS	Michelson Interferometer for Passive Atmospheric Sounding
IASI-(NG)	Infrared Atmospheric Sounding Interferometer—(New Generation)
EUMETSAT	European Organisation for the Exploitation of Meteorological Satellites
CNES	Centre national d'études spatiales
MTG-S	Meteosat Third Generation—Sounding
EE	Earth Explorer
FORUM	Far-infrared Outgoing Radiation Understanding and Monitoring
CAIRT	Changing Atmosphere Infrared Tomography
FOV	Field Of View
GLORIA	Gimballed Limb Observer for Radiance Imaging of the Atmosphere
DIRSIG	Digital Imaging and Remote Sensing Image Generation
GIIRS	Geostationary Interferometric Infrared Sounder
FTIR-SIS	Fourier Transform InfraRed Scientific Instrument Simulator
FIRI	Far Infra-Red Interferometer
SHIFTS	Simulator for the Herschel Imaging Fourier Transform Spectrometer
SPIRE	Spectral and Photometric Imaging Receiver
WFE	Wavefront Error
PRNU	Pixel Response Non-Uniformity
LOS	Line of Sight
ILS	Instrument Line Shape
UV	Ultraviolet
FT	Front Telescope
IA	Interferometer Assembly
BT	Back Telescope
CW	Cryostat Window
DU	Detection Unit
ADC	Analogue-to-Digital Converter
BSU	Beam Splitter Unit
CC	Cube Corner
OPD	Optical Path Difference
ZPD	Zero-Path Difference
BS	Beam-splitting Surface
BP	Beam-splitting Plate
CP	Compensating Plate

AR	Anti-Reflective
QE	Quantum Efficiency
CHC	Charge-Handling Capacity
LSB	Least Significant Bit
DC	Unmodulated
AC	Modulated
MOPD	Maximum Optical Path Difference
FWHM	Full Width at Half Maximum
NESR	Noise-Equivalent Spectral Radiance
NEDT	Noise-Equivalent Differential Temperature
KIT	Karlsruher Institut für Technologie
FZJ	Forschungszentrum Jülich
MCT	Mercury Cadmium Telluride
LFPA	Large Focal Plane Array
PTB	Physikalisch-Technische Bundesanstalt
VLWIR	Very Long-Wave Infrared
SF_6	Sulphur Hexafluoride
O_3	Ozone
SO_2	Sulphur dioxide
σ	Wavenumber
α	Bulk absorption coefficient
β	Material bulk absorption rate
h	Optical thickness
d	Mechanical thickness
ϕ	Beam incidence angle
n	Optical index
N	Signal
ρ	Pixel fill-factor
τ_{int}	Integration time
η	Quantum efficiency
$hc\sigma$	Photon energy
F	Spectral flux
δ	Optical path difference
O	Instrument function
M	Modulation efficiency
$R\{.\}$	Real part operator
$FT\{.\}$	Fourier Transform operator
I_{dark}	Pixel dark current density
p_x	Horizontal pixel pitch
p_y	Vertical pixel pitch
R_V	Voltage response
f_{el}	Electric frequency
v_{opt}	Optical speed
f_{acq}	Acquisition frequency
ξ	Noise standard deviation
b	Binning factor
L	Spectral radiance
G	Optical etendue
K	Optical transmission
R	Reflectivity
ε	Emissivity
T	Temperature
A_{DU}	Studied active detection area
$J_1()$	Bessel function of first kind

γ_{tilt}	Angular tilt between interfering wavefronts
R_{stop}	Aperture stop equivalent radius
γ_{shear}	Shear between interfering wavefronts
Ω	Beam solid angle
$\langle . \rangle$	Average operator
$\Delta\delta^2$	Differential wavefront error between interfering wavefronts
θ_0	Beam off-axis angle with respect to field of view centre
MOPD	Maximum optical path difference
ILS	Instrument line shape
M_{ifg}	Interferogram number of samples
$d\sigma$	Spectral sampling
NESR	Noise-equivalent spectral radiance
NEDT	Noise-equivalent differential temperature
G	Radiometric gain
L_0	Radiometric offset

Appendix A. Interferometer Self-Emission

The IA self-emission scheme is represented in Figure A1. The flux of any beam of light which is split and recombined by the BS is modulated. The IA emissivity includes six contributions described hereafter. Each component emissivity includes the transmission factor from itself to the output port of the interferometer.

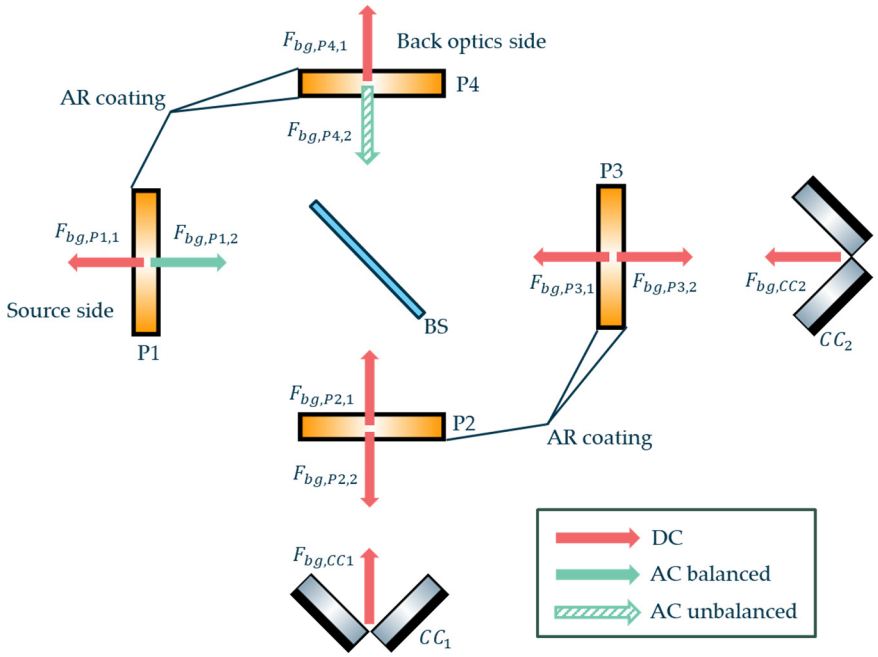

Figure A1. Thermal background emission in the interferometer with a distinction between the DC flux (red), AC balanced flux (full green), and AC unbalanced (dashed green). This sketch was created using the Component Library by Alexander Franzen, licensed under CC BY-NC 3.0.

P_1 is located right before the beam-splitting surface. A fraction of its self-emission $F_{bg,P1,1}$ goes back to the source side while the other $F_{bg,P1,2}$ is modulated:

$$F_{bg,P1}(\sigma,\delta) = G\left[\varepsilon_{P1,DC}(\sigma) + \varepsilon_{P1,AC}(\sigma)\right] L_{BB}(T_{IA},\sigma) \tag{A1}$$

where

$$\varepsilon_{P1,DC}(\sigma) = \frac{(1-\alpha_{BP})K_{IA,DC}}{\alpha_{BP}K_{AR}}(\sigma) \tag{A2}$$

and

$$\varepsilon_{P1,AC}(\sigma) = \frac{(1-\alpha_{BP})K_{IA,AC}}{\alpha_{BP}K_{AR}}(\sigma) \tag{A3}$$

The P_2 self-emission $F_{bg,P2}$ is split but not recombined; it is thus unmodulated and is computed as follows:

$$F_{bg,P2}(\sigma,\delta) = G\varepsilon_{P2}(\sigma)L_{BB}(T_{IA},\sigma) \tag{A4}$$

where

$$\varepsilon_{P2}(\sigma) = (1-\alpha_{BP})\Big[\, R_{CC1}\alpha_{BP}K_{BS}\alpha_{CP}K_{AR}^3\Big] + (1-\alpha_{BP}K_{AR})\Big[\, K_{BS}\alpha_{CP}K_{AR}^2\,\Big](\sigma) \tag{A5}$$

The P_3 self-emission $F_{bg,P3}$ is split but not recombined, it is thus unmodulated and is computed as follows:

$$F_{bg,P3}(\sigma,\delta) = G\varepsilon_{P3}(\sigma)L_{BB}(T_{IA},\sigma) \tag{A6}$$

where

$$\varepsilon_{P3}(\sigma) = (1-\alpha_{CP})\Big[\, R_{CC2}\alpha_{CP}^2K_{AR}^4 + R_{BS}\alpha_{CP}K_{AR}^2\,\Big](\sigma) \tag{A7}$$

P_4 is located after the recombination point. Its self-emission is composed by the flux emitted directly towards the back optics side $F_{bg,P4,1}$ but also emitted towards the interferometer and reflected to the back optics side. This part $F_{bg,P4,2}$ is modulated in phase opposition to the source.

$$F_{bg,P4}(\sigma,\delta) = G[\varepsilon_{P4,DC}(\sigma) + \varepsilon_{P4,AC}(\sigma)\Big]L_{BB}(T_{IA},\sigma) \tag{A8}$$

where

$$\varepsilon_{P4,DC}(\sigma) = (1-\alpha_{CP})\left[K_{AR} + \frac{R_{IA,DC}}{\alpha_{CP}K_{AR}}\right](\sigma) \tag{A9}$$

and

$$\varepsilon_{P4,AC}(\sigma) = (1-\alpha_{CP})\frac{R_{IA,AC}}{\alpha_{CP}K_{AR}}(\sigma) \tag{A10}$$

The thermal background coming from the CCs is unmodulated and expressed as follows:

$$F_{bg,CC}(\sigma,\delta) = G[\varepsilon_{CC1}(\sigma) + \varepsilon_{CC2}(\sigma)]L_{BB}(T_{IA},\sigma) \tag{A11}$$

where

$$\varepsilon_{CC1}(\sigma) = (1-R_{CC1})\alpha_{BP}K_{BS}\alpha_{CP}K_{AR}^3(\sigma) \tag{A12}$$

and

$$\varepsilon_{CC2}(\sigma) = (1-R_{CC2})R_{BS}\alpha_{CP}^2K_{AR}^4(\sigma) \tag{A13}$$

The IA total unmodulated $\varepsilon_{IA,DC}$ emissivity writes as follows: the balanced modulated $\varepsilon_{IA,AC,1}$ and unbalanced modulated $\varepsilon_{IA,AC,2}$, as follows:

$$\varepsilon_{IA,DC}(\sigma) = [\varepsilon_{P1,DC} + \varepsilon_{P2} + \varepsilon_{P3} + \varepsilon_{P4,DC} + \varepsilon_{CC1} + \varepsilon_{CC2}](\sigma) \tag{A14}$$

The IA total balanced modulated $\varepsilon_{IA,AC,1}$ emissivity writes as follows:

$$\varepsilon_{IA,AC,1}(\sigma) = \varepsilon_{P1,AC}(\sigma) \tag{A15}$$

The IA total unbalanced modulated $\varepsilon_{IA,AC,2}$ emissivity writes as follows:

$$\varepsilon_{IA,AC,2}(\sigma) = \varepsilon_{P4,AC}(\sigma) \tag{A16}$$

Appendix B. Radiometric Gain and Offset Noise

The radiometric gain noise standard deviation ξ_G is as follows:

$$\xi_G(\sigma) = \sqrt{\xi_{\sigma,1}^2 \left| \frac{\partial G(\sigma)}{\partial N_{\sigma,1}(\sigma)} \right|^2 + \xi_{\sigma,2}^2 \left| \frac{\partial G(\sigma)}{\partial N_{\sigma,2}(\sigma)} \right|^2} \tag{A17}$$

thus yielding

$$\xi_G(\sigma) = \sqrt{\xi_{\sigma,1}^2 \left| \frac{L_1(\sigma) - L_2(\sigma)}{(N_{\sigma 1}(\sigma) - N_{\sigma,2}(\sigma))^2} \right|^2 + \xi_{\sigma,2}^2 \left| \frac{L_1(\sigma) - L_2(\sigma)}{(N_{\sigma,1}(\sigma) - N_{\sigma,2}(\sigma))^2} \right|^2} \tag{A18}$$

considering the relation between G, ξ_σ, and the NESR (Equation (57))

$$\xi_G(\sigma) = \sqrt{\frac{NESR_1^2(\sigma) + NESR_2^2(\sigma)}{|\, N_{\sigma,1}(\sigma) - N_{\sigma,2}(\sigma)\,|^2}} \tag{A19}$$

The radiometric offset ξ_{L0} noise standard deviation is as follows:

$$\xi_{L_0}(\sigma) = \sqrt{\xi_{\sigma,1}^2 \left| \frac{\partial L_0(\sigma)}{\partial N_{\sigma,1}(\sigma)} \right|^2 + \xi_{\sigma,2}^2 \left| \frac{\partial L_0(\sigma)}{\partial N_{\sigma,2}(\sigma)} \right|^2} \tag{A20}$$

which, after calculation, writes as follows:

$$\xi_{L_0}(\sigma) = \sqrt{\xi_{\sigma,1}^2 \left| N_{\sigma,2}(\sigma) \frac{L_1(\sigma) - L_2(\sigma)}{(N_{\sigma,1}(\sigma) - N_{\sigma,2}(\sigma))^2} \right|^2 + \xi_{\sigma,2}^2 \left| N_{\sigma,1}(\sigma) \frac{L_1(\sigma) - L_2(\sigma)}{(N_{\sigma,1}(\sigma) - N_{\sigma,2}(\sigma))^2} \right|^2} \tag{A21}$$

thus yielding

$$\xi_{L_0}(\sigma) = \sqrt{\left[\left| \frac{L_0(\sigma) + L_2(\sigma)}{L_1(\sigma) - L_2(\sigma)} \right| NESR_1(\sigma) \right]^2 + \left[\left| \frac{L_0(\sigma) + L_1(\sigma)}{L_1(\sigma) - L_2(\sigma)} \right| NESR_2(\sigma) \right]^2} \tag{A22}$$

References

1. Davis, S.P.; Abrams, M.C.; Brault, J.W. Why choose a Fourier transform spectrometer? In *Fourier Transform Spectrometry*; Academic Press: Cambridge, MA, USA, 2001.
2. Peter, G.; James, H. *Fourier Transform Infrared Spectrometry*, 2nd ed.; John Wiley & Sons, Inc.: Hoboken, NJ, USA, 2006.
3. Fischer, H.; Birk, M.; Blom, C.; Carli, B.; Carlotti, M.; von Clarmann, L.; Delbouille, A.; Dudhia, D.; Ehhalt, M.; Endemann, J.M.F.; et al. MIPAS: An Instrument for Atmospheric and Climate Research. *Atmos. Chem. Phys.* **2008**, *8*, 2151–2188. [CrossRef]
4. Clerbaux, C.; Boynard, A.; Clarisse, L.; George, M.; HadjiLazaro, J.; Herbin, H.; Hurtmans, D.; Pommier, M.; Razavi, A.; Turquety, S.; et al. Monitoring of Atmospheric Composition Using the Thermal Infrared IASI/MetOp Sounder. *Atmos. Chem. Phys.* **2009**, *9*, 6041–6054. [CrossRef]
5. Abdon, S.; Riegger, L.; Pedone, G.; Finella, E.; Sheard, B.; Giraud, J.; Guggenmoser, T.; Lamarre, D.; Den, V.; Fowler, G.; et al. Meteosat Third-Generation IRS Sounding Mission Development Status and Test Results. In Proceedings of the International Conference on Space Optics—ICSO 2024, Antibes Juan-les-Pins, France, 21–25 October 2024; SPIE: Bellingham, WA, USA, 2025; Volume 13699, p. 136990B.
6. Bernard, F.; Calvel, B.; Pasternak, F.; Davancens, R.; Buil, C.; Baldit, E.; Luitot, C.; Penquer, A. Overview of IASI-NG the New Generation of Infrared Atmospheric Sounder. In Proceedings of the International Conference on Space Optics—ICSO 2014, Canary Islands, Spain, 6–10 October 2014; SPIE: Bellingham, WA, USA, 2017; Volume 10563, p. 105633H.
7. The European Space Agency. Earth Explorer 9 Candidate Mission FORUM—Report for Mission Selection. 2019. Available online: https://esamultimedia.esa.int/docs/EarthObservation/EE9-FORUM-RfMS-ESA-v1.0-FINAL.pdf (accessed on 23 June 2025).
8. The European Space Agency. EARTH EXPLORER 11 Candidate Mission NITROSAT Report for Assessment. 2023. Available online: https://esamultimedia.esa.int/docs/EarthObservation/EE11_Nitrosat_Report_for_Assessment_v1.0_15Sept23.pdf (accessed on 23 June 2025).

9. The European Space Agency. EARTH EXPLORER 11 Candidate Mission CAIRT Report for Assessment. 2023. Available online: https://esamultimedia.esa.int/docs/EarthObservation/EE11_CAIRT_Report_for_Assessment_v1.0_15Sept23.pdf (accessed on 23 June 2025).
10. The European Space Agency. ESA Graduate Trainees. Available online: https://www.esa.int/About_Us/Careers_at_ESA/Graduates_ESA_Graduate_Trainees?ci_id=599&client_id=43&college=6&grad_trainingDir=DESC&grad_trainingOrder=Sorter_description&jobholder_id=448&lang_coursesDir=DESC&lang_coursesOrder=Sorter_college_id&lang_coursesPage=10&sector_id=32 (accessed on 13 May 2025).
11. Friedl-Vallon, F.; Gulde, T.; Hase, F.; Kleinert, A.; Kulessa, T.; Maucher, G.; Neubert, T.; Olschewski, F.; Piesch, C.; Preusse, P.; et al. Instrument Concept of the Imaging Fourier Transform Spectrometer GLORIA. *Atmos. Meas. Tech.* **2014**, *7*, 3565–3577. [CrossRef]
12. Alain, F. Simulation of Imaging Fourier Transform Spectrometers Using DIRSIG. 1999. Available online: https://dirsig.cis.rit.edu/docs/alain.pdf (accessed on 23 June 2025).
13. Weiner, A.M.; Messinger, D.W. An end-to-end Airborne FTS Simulation for Evaluating the Performance Trade Space in Fugitive Gas Identification. In Proceedings of the Imaging Spectrometry XV, San Diego, CA, USA, 1–5 August 2010; SPIE: Bellingham, WA, USA; Volume 7812, p. 78120T.
14. Zhang, W.; Zhang, B.; Gao, L.; Zhang, W. Image Simulator for Spatially Imaging Fourier Transform Spectrometer "HJ1A-HSI". In Proceedings of the Sensors, Systems, and Next-Generation Satellites XIV, Toulouse, France, 20–23 September 2010; SPIE: Bellingham, WA, USA, 2010; Volume 7826, p. 78262P.
15. Erik, K. Modelling of the Instrument Spectral Response of Conventional and Imaging Fourier Transform Spectrometers, Laval. 2014. Available online: https://corpus.ulaval.ca/entities/publication/14d279a4-25e2-4418-922a-6003aae3d8f2 (accessed on 23 June 2025).
16. Ni, Z.; Lu, Q.; Xu, Y.; Huo, H. Intensity Simulation of a Fourier Transform Infrared Spectrometer. *Sensors* **2020**, *20*, 1833. [CrossRef]
17. Sermania, B.; VanFossen, N.; Steen, R.; Stewart, M.; Raston, P.L. FTIR-SIS: A Fourier Transform Infrared Scientific Instrument Simulator. *J. Chem. Educ.* **2024**, *101*, 1711–1717. [CrossRef]
18. Juanola-Parramon, R.; Savini, G.; Fenech, D.; Walsh, C. An end-to-end Far-infrared Interferometer Instrument Simulator (FIInS). In Proceedings of the Space Telescopes and Instrumentation 2014: Optical, Infrared, and Millimeter Wave, Montréal, QB, USA, 22–27 June 2014; SPIE: Bellingham, WA, USA, 2014; Volume 9143, p. 91434I.
19. Lindner, J.V.; Naylor, D.A.; Swinyard, B.M. SHIFTS: Simulator for the Herschel imaging Fourier transform spectrometer. In Proceedings of the Space Telescopes and Instrumentation I: Optical, Infrared, and Millimeter, Orlando, FL, USA, 24–31 May 2006; SPIE: Bellingham, WA, USA, 2006; Volume 6265, p. 62652Y.
20. Perron, G.P.; Moreau, L.M.; Miras, D.; Chetrite, B. IASI Simulation Model. In Proceedings of the Sensors, Systems, and Next-Generation Satellites VI, Toronto, ON, Canada, 24–28 June 2002; SPIE: Bellingham, WA, USA, 2003; Volume 4881.
21. Vicent, J.; Verrelst, J.; Sabater, N.; Alonso, L.; Rivera-Caicedo, J.P.; Martino, L.; Muñoz-Marí, J.; Moreno, J. Comparative analysis of atmospheric radiative transfer models using the Atmospheric Look-up table Generator (ALG) toolbox (version 2.0). *Geosci. Model Dev.* **2020**, *13*, 1945–1957. [CrossRef]
22. Clough, S.A.; Shephard, M.W.; Mlawer, E.J.; Delamere, J.S.; Iacono, M.J.; CadyPereira, K.; Boukabara, S.; Brown, P.D. Atmospheric Radiative Transfer Modeling: A Summary of the AER Codes. *J. Quant. Spectrosc. Radiat. Transf.* **2005**, *91*, 233–244. [CrossRef]
23. Mitchell, H.J.; Hemmer, T.H.; Lewis, P.E.; Salvaggio, C. Effects of Temporally Changing Sources on Fourier Transform Spectrometers. In Proceedings of the Aerospace/Defense Sensing, Simulation, and Controls, Orlando, FL, USA, 16–20 April 2001; SPIE: Bellingham, WA, USA, 2001; Volume 4381, pp. 516–526.
24. Kyle, T.G.; Blatherwick, R. Smearing of Interferograms in Fourier Transform Spectroscopy. *Appl. Opt.* **1984**, *23*, 261–263. [CrossRef] [PubMed]
25. Daniels, A. *Field Guide to Infrared Systems, Detectors, and FPAs*; SPIE: Bellingham, WA, USA, 2018.
26. Revercomb, H.E.; Buijs, H.; Howell, H.B.; LaPorte, D.D.; Smith, W.L.; Sromovsky, L.A. Radiometric Calibration of IR Fourier Transform Spectrometers: Solution to a Problem with the High-Resolution Interferometer Sounder. *Appl. Opt.* **1988**, *27*, 3210–3218. [CrossRef]
27. Hearn, D.R. *Fourier Transform Interferometry*; MIT: Cambridge, MA, USA, 1999. Available online: https://apps.dtic.mil/sti/pdfs/ADA370423.pdf (accessed on 28 June 2025).
28. Davis, S.P.; Abrams, M.C.; Brault, J.W. Nonideal (real-world) interferograms. In *Fourier Transform Spectrometry*; Academic Press: Cambridge, MA, USA, 2001.
29. Chase, D.B. Nonlinear Detector Response in FT-IR. *Appl. Spectrosc.* **1984**, *38*, 491–494. [CrossRef]
30. Teledyne, Pattern Noise: DSNU and PRNU. Available online: https://www.teledynevisionsolutions.com/learn/learning-center/imaging-fundamentals/pattern-noise-dsnu-and-prnu/ (accessed on 7 May 2025).
31. Chen, X.; Tan, Z.; Zhao, N.; Wang, J.; Liu, Y.; Tang, Y.; He, P.; Li, W.; Sun, J.; Si, J.; et al. Suitable Integral Sampling for Bandpass-Sampling Time-Modulated Fourier Transform Spectroscopy. *Appl. Sci.* **2024**, *14*, 1009. [CrossRef]

32. Bennett, C.L. Effect of Jitter on an Imaging FTIR Spectrometer. In Proceedings of the Infrared Imaging Systems: Design, Analysis, Modeling, and Testing VIII, Orlando, FL, USA, 21–25 April 1997; SPIE: Bellingham, WA, USA, 1997; Volume 3063, pp. 174–184.
33. Bell, E.; Sanderson, R. Spectral Errors Resulting from Random Sampling-Position Errors in Fourier Transform Spectroscopy. *Appl. Opt.* **1972**, *11*, 688–689. [CrossRef]
34. Flunger, J.; Buisset, C.; Friedl-Vallon, F.; Hoffmann, A.; Kleinert, A.; Malavart, A.; Mazeau, V.; Piekarski, T. Independent Performance Validation of the Instrument Simulator Model of CAIRT's End to End Performance Simulator. In Proceedings of the Living Planet Symposium, Vienna, Austria, 23–27 June 2025. Available online: https://lps25.esa.int/lps25-presentations/poster/Independent%20Performance%20Validation%20of%20the%20Instrument%20Simulator%20Model%20of%20CAIRT%e2%80%99s%20End%20to%20End%20Performance%20Simulator.pdf (accessed on 23 June 2025).
35. Piekarski, T.; Buisset, C.; Friedl-Vallon, F.; Kleinert, A.; Heliere, A.; Hofmann, J.; Babic, L.; Dias Miranda, M.; Guggenmoser, T.; Lamarre, D.; et al. A versatile Fourier transform spectrometer model for future Earth observation missions. In Proceedings of the Living Planet Symposium, Vienna, Austria, 23–27 June 2025. Available online: https://lps25.esa.int/lps25-presentations/presentations/203/Piekarski_update.pdf (accessed on 26 November 2025).
36. Taylor, J.K.; Revercomb, H.E.; Best, F.A.; Tobin, D.C.; Gero, P.J. The Infrared Absolute Radiance Interferometer (ARI) for CLARREO. *Remote Sens.* **2020**, *12*, 1915. [CrossRef]
37. Larson, W.J.; Wertz, J.R. *Space Mission Analysis and Design*, 3rd ed.; Space Technology Library: Berlin/Heidelberg, Germany, 1999.
38. Hecht, E. *Optics*, 5th ed.; Pearson Deutschland GmbH: Munich, Germany, 2016.
39. Buss, D.D.; Kansy, R.J.; Barton, J.B. KTC Noise on Direct Injection from IR Diodes. *IEEE Trans. Electron. Dev.* **1980**, *27*, 998–1000. [CrossRef]
40. Rogalski, A. Pyroelectric detectors. In *Infrared Detectors*, 2nd ed.; Taylor and Francis Group and CRC Press: Boca Raton, FL, USA, 2010.
41. Redd, J.D. *Alternative Beam Splitter/Compensator Configurations for Reduction of Multiple Reflections in Imaging Fourier Transform Spectrometers*; University of Utah: Salt Lake City, UT, USA, 1998. Available online: https://digitalcommons.usu.edu/spacegrant/1998/Session2/1/ (accessed on 5 June 2025).
42. Smith, D.; Hunt, S.E.; Etxaluze, M.; Peters, D.; Nightingale, T.; Mittaz, J.; Woolliams, E.R.; Polehampton, E. Traceability of the Sentinel-3 SLSTR Level-1 Infrared Radiometric Processing. *Remote Sens.* **2021**, *13*, 374. [CrossRef]
43. Yang, S.; Vayyshenker, I.; Li, X.; Scott, T.R. Accurate Measurement of Optical Detector Nonlinearity. Natl. Inst. Stand. Technol., Tech. Note 1376, Boulder, CO, USA. 1995. Available online: https://nvlpubs.nist.gov/nistpubs/Legacy/TN/nbstechnicalnote1376.pdf (accessed on 5 July 2025).
44. Schott, J.R. Magic π. In *Remote Sensing: The Image Chain Approach*; Oxford University Press: Oxford, NY, USA, 2007.
45. Davis, S.P.; Abrams, M.C.; Brault, J.W. Theory of the ideal instrument. In *Fourier Transform Spectrometry*; Academic Press: San Diego, CA, USA, 2001.
46. Martino, A.J.; Hagopian, J.G. Effects of Shear, Defocus, and Wavefront Error on the Theoretical Performance of the Composite Infrared Spectrometer for Cassini. In Proceedings of the International Symposium on Optical Science, Engineering, and Instrumentation, San Diego, CA, USA, 19–24 July 1998; SPIE: Bellingham, WA, USA, 1998; Volume 3435, pp. 52–60.
47. Davis, S.P.; Abrams, M.C.; Brault, J.W. Effects of noise in its various forms. In *Fourier Transform Spectrometry*; Academic Press: San Diego, CA, USA, 2001.
48. Kruse, P.W. Noise equivalent temperature difference. In *Uncooled Thermal Imaging: Arrays, Systems, and Applications*; SPIE: Bellingham, WA, USA, 2002.
49. Kleinert, A.; Friedl-Vallon, F.; Guggenmoser, T.; Höpfner, M.; Neubert, T.; Ribalda, R.; Sha, M.K.; Ungermann, J.; Blank, J.; Ebersoldt, A.; et al. Level 0 to 1 processing of the imaging Fourier transform spectrometer GLORIA: Generation of radiometrically and spectrally calibrated spectra. *Atmos. Meas. Tech.* **2014**, *7*, 4167–4184. [CrossRef]
50. Sromovsky, L.A. Radiometric Errors in Complex Fourier Transform Spectrometry. *Appl. Opt.* **2003**, *42*, 1779–1787. [CrossRef]
51. Friedl-Vallon, F.; Kretschmer, E.; Neuber, T.; Ungermann, J.; Hopfner, M.; Gulde, T.; Johansson, S.; Kleinert, A.; Maucher, G.; Piesch, C.; et al. First Flight—First Light: The Novel Limb-Imaging FTIR Sounder GLORIA-Lite Crossing the Atlantic. In Proceedings of the Living Planet Symposium, Vienna, Austria, 23–27 June 2025. Available online: https://lps25.esa.int/lps25-presentations/presentations/200/_200.pdf (accessed on 26 November 2025).
52. Kleinert, A.; Krisch, I.; Ungermann, J.; Adibekyan, A.; Gutschwager, B.; Monte, C. Characterization of Blackbody Inhomogeneity and Its Effect on the Retrieval Results of the GLORIA Instrument. *Atmos. Meas. Tech.* **2018**, *11*, 3871–3882. [CrossRef]
53. Ungermann, J.; Kleinert, A.; Maucher, G.; Bartolomé, I.; Friedl-Vallon, F.; Johansson, S.; Krasauskas, L.; Neubert, T. Quantification and mitigation of the instrument effects and uncertainties of the airborne limb imaging FTIR GLORIA. *Atmos. Meas. Tech.* **2022**, *15*, 2503–2530. [CrossRef]

54. Hanna, S.; Bitterlich, H.; Breiter, R.; Eich, D.; Epping, A.; Figgemeier, H.; Lutz, H.; Mahlein, K.M.; Ullrich, M.; Sieck, A. HOT all the way from SWIR to VLWIR at AIM: Present status of MCT-based small pitch infrared detector arrays for higher operating temperatures and the shape of things to come. In Proceedings of the Infrared Technology and Applications L, National Harbor, ML, USA, 21–25 April 2024; SPIE: Bellingham, WA, USA, 2024; Volume 13046, p. 130460F.
55. Rogalski, A.; Hu, W.; Wang, F.; Martyniuk, P. Performance of Low-Dimensional Solid Room-Temperature Photodetectors—Critical View. *Materials* **2024**, *17*, 4522. [CrossRef] [PubMed]
56. Hirschfeld, T. Multiple Order Spectra in Fourier Transform Infrared Spectroscopy. *Appl. Opt.* **1977**, *16*, 1905–1907. [CrossRef] [PubMed]
57. Blumenstock, T.; Hase, F.; Keens, A.; Czurlok, D.; Colebatch, O.; Garcia, O.; Griffith, D.W.T.; Grutter, M.; Heikkinen, J.W.; Jeseck, P.; et al. Characterization and Potential for Reducing Optical Resonances in Fourier Transform Infrared Spectrometers of the Network for the Detection of Atmospheric Composition Change (NDACC). *Atmos. Meas. Tech.* **2021**, *14*, 1239–1252. [CrossRef]
58. Moazzami, K.; Phillips, J.; Lee, D.; Krishnamurthy, S.; Benoit, G.; Fink, Y.; Tiwald, T. Detailed Study of above Bandgap Optical Absorption in HgCdTe. *J. Electron. Mater.* **2005**, *34*, 773–778. [CrossRef]
59. Forschungszentrum Jülich, F. Infrared Reference Spectra. Available online: https://datapub.fz-juelich.de/slcs/spectra/html/view_limb_20km_day_C2H2.html (accessed on 2 July 2025).
60. Wetzel, G.; Kleinert, A.; Johansson, S.; Friedl-Vallon, F.; Höpfner, M.; Ungermann, J.; Neubert, T.; Catoire, V.; Crevoisier, C.; Engel, A.; et al. Intercomparison and validation of first GLORIA-B measurements of stratospheric and upper tropospheric long-lived tracers and photochemically active species. *EGUsphere* **2025**, *18*, 5873–5894. [CrossRef]
61. Norton, R.H.; Beer, R. Errata: New Apodizing Functions for Fourier Spectrometry. *J. Opt. Soc. Am.* **1977**, *67*, 419. [CrossRef]
62. Pachot, C.; Dominguez, B.C.; Oetjen, H.; Sierk, B.; Mariani, F.; Riel, S.; Rodrigues, G.; Copano, M.; Carou, A.M.; Palchetti, L.; et al. The Infrared Fourier Transform Spectrometer and the Infrared Imager Instrument Concepts for the FORUM Mission, ESA's 9th Earth Explorer. In Proceedings of the Sensors, Systems, and Next-Generation Satellites XXIV, Online, 21–25 September 2020; SPIE: Bellingham, WA, USA, 2020; Volume 11530, p. 115300D.

Disclaimer/Publisher's Note: The statements, opinions and data contained in all publications are solely those of the individual author(s) and contributor(s) and not of MDPI and/or the editor(s). MDPI and/or the editor(s) disclaim responsibility for any injury to people or property resulting from any ideas, methods, instructions or products referred to in the content.